

Research Article

Fracture, Dissolution, and Cementation Events in Ordovician Carbonate Reservoirs, Tarim Basin, NW China

Vinyet Baqués , Estibalitz Ukar, Stephen E. Laubach, Stephanie R. Forstner, and Andrés Fall

Bureau of Economic Geology, Jackson School of Geosciences, The University of Texas at Austin, University Station Box X Austin, TX 78713-8924, USA

Correspondence should be addressed to Vinyet Baqués; vinyetb@gmail.com

Received 18 October 2019; Revised 12 January 2020; Accepted 14 February 2020; Published 18 April 2020

Guest Editor: Enrique Gomez-Rivas

Copyright © 2020 Vinyet Baqués et al. This is an open access article distributed under the Creative Commons Attribution License, which permits unrestricted use, distribution, and reproduction in any medium, provided the original work is properly cited.

Ordovician carbonate rocks of the Yijianfang Formation in the Tabei Uplift, Tarim Basin, contain deeply buried (>6000 m), highly productive oil and gas reservoirs associated with large cavities (>10 m). Previous workers inferred that large cavities are paleocaves (paleokarst) formed near the surface and subsequently buried. Alternately, caves may have formed by dissolution at depth along faults. Using 227 samples from 16 cores, we document textures and cement compositions bearing on cavity histories with petrographic, high-resolution scanning electron microscopy (SEM), isotopic, and fluid inclusion microthermometric observations. Results show that dissolution occurred at depth and was caused by (1) acidic fluids derived from Middle-Late Silurian and/or Devonian-Permian hydrocarbon generation and maturation, (2) high-temperature fluids, of which some were associated with Late Permian igneous activity, and (3) Mg-rich fluids that accompanied Jurassic-Cretaceous deformation and the formation of partially open fractures and stylobreccias (fault breccias). The relative paragenetic sequence of the structure-related diagenesis suggests seven stages of fracturing, dissolution, and cementation. Mottle fabrics in the Yijianfang Formation contain argillaceous carbonate-rich silt and are bioturbation features formed within the marine environment. Those mottled fabrics differ from clearly karstic features in the overlying Lianglitage Formation, which formed by near-surface dissolution and subsequent infilling of cavities by allochthonous sediment. Mottle fabrics are crosscut by compacted fractures filled with phreatic-vadose marine cements and followed by subsequent generations of cement-filled fractures and vugs indicating that some fractures and vugs became cement filled prior to later dissolution events. Calcite cements in fractures and vugs show progressively depleted values of $\delta^{18}\text{O}$ documenting cement precipitation within the shallow (~220 m), intermediate (~625 m), and deep (~2000 m) diagenetic environments. Deep (mesogenetic) dissolution associated with fractures is therefore the principal source of the high porosity-permeability in the reservoir, consistent with other pieces of evidence for cavities localized near faults.

1. Introduction

Giant volumes of oil and gas are contained in Ordovician carbonate rocks of the Tarim Basin, NW China, especially in the Tabei Uplift, where proven oil/gas reserves surpass 3 billion tonnes of oil-equivalent [1]. Well drilling responses such as bit drops and mud losses indicate that high-porosity and high-permeability zones, including large (>10 m) cavities, are present in deeply buried (>6000 m) reservoirs [2–5]. Many economic carbonate reservoirs are housed in rocks

that preserve early dissolution porosity produced by meteoric diagenesis—karstification—prior to significant burial [6–12]. However, in many settings, increasing evidence supports the formation of secondary porosity during late deep-burial conditions (mesogenetic; discussed by Giles and Marshall [13], Mazzullo and Harris [14], and Wright and Harris [15]) by corrosive diagenetic fluids of diverse nature [16–20].

The origin of the deep pore networks in carbonate rocks of the Yijianfang Formation in the central Tarim Basin is debated [4, 5, 21–23]. Karstic features are present in Middle Ordovician

carbonates within the nearby Lunnan and Tahe oilfields [2, 24–27]. Here, cavities have been linked to a hiatus of as much as 120 m.y. prior to deposition of Silurian siliciclastic rocks [2, 25, 28]. In the paleostructurally lower Halahatang area, however, a well-defined unconformity is absent [29, 30]. The main evidence for near-surface karst is the so-called mottled fabric, a texture very common within the Yijianfang Formation. This feature has been interpreted to be near-surface paleokarst breccia or sediment-filled vugs/cavities [31–34] but has recently been brought into question [22, 35]. Additionally, regional structural interpretation and fault mapping in the Halahatang area reveal a network of conjugate strike-slip fault systems that developed damage zones which has a good agreement with the high well production [36, 37]. Wu et al. [37] hint that there is much more dissolution developed along the fault damage zones, suggesting that fluid pathways formed in those areas facilitate the later dissolution in the fault zones. The fracture-cave reservoirs are quite different from the high-matrix reservoirs and meteoric karst reservoirs [9, 38] but are strongly heterogeneous reservoirs that are close to mesogenetic dissolution or hydrothermal karstification along fault zones [14, 21, 39].

Dissolution processes partially or completely eliminate original microstratigraphic and textural records. Precipitated cements on the other hand, especially precorrosion and post-dissolution minerals filling cavities and fractures, may record information on the elemental and isotopic chemistry of dissolving fluids involved in structural diagenetic events [40]. Cements provide information on the physical and chemical conditions of the reservoir during different stages of diagenesis, as well as the composition of fluids, and allow obtaining information that would otherwise be unavailable from empty voids. Sequences of crosscutting cements and fluid inclusions trapped within them can provide insights into the origin, types, and pathways of fluids as well as depths of dissolution and cementation events over time [41–44]. We used petrography, scanning electron microscopy (SEM), C, O, and Sr isotopes, and fluid inclusion microthermometry of core samples from 16 wells in the Halahatang oilfield to establish the paragenetic sequence, temperature conditions, and origins of the fluids and events that led to the formation of cryptic mottle textures as well as dissolution vugs and fractures within these deeply buried (5500 to 7500 m) Ordovician carbonate reservoirs.

Here, we show that deep (mesogenetic) dissolution associated with fractures is the principal source of currently open cavities in the reservoir. Mottle fabrics are not the result of penetrative karstic processes but represent burrows that were later overprinted by mesogenetic dissolution. We found no evidence for pervasive near-surface dissolution. We document seven stages of overprinted fracturing and dissolution, with evidence for precipitation of cements from the marine to deep diagenetic environments. Stable isotopic analyses tied to geothermal gradients indicate most of the dissolution that predated each additional fracture-dissolution event occurred within the mesogenetic environment (220–2000 m). Dissolution was caused in various stages by a range of fluids, including meteoric and organic acids and high-temperature and Mg-rich fluids.

2. Geological Setting

The Tarim Basin is the largest cratonic area in western China covering an area of nearly 600,000 km² (Figure 1). The basin is bounded by the Tian Shan Mountains to the northwest, Kuluketage region to the northeast, Kunlun Mountains to the south and southwest, and Altyn Fault Zone to the southeast (Figure 1). Its Precambrian crystalline basement represents a fragment of the Rodinia supercontinent that has undergone long-term geological evolution from the Sinian (latest Neoproterozoic) to the Neogene [45, 46]. Except for flood basalts of the Tarim Igneous Province at ~290 Ma [47] (Figure 1), the evolution of the Tarim Basin is characterized by almost continuous sedimentation since the Neoproterozoic. Long-term polycyclic tectonic evolution of the Tarim Basin resulted in the formation of three paleohighs (Tabei, Central Tazhong, and Southeast Tadong) and four depressions (Kuqa, Manjiaer, Southwest Tangguzibasi, and Southeast Tadong) [45, 48–54] (Figure 1). During the Late Sinian–Early Ordovician period, the Tarim Basin was under extension resulting in a series of normal faults and horst-graben structures [45, 55, 56]. The passive continental margin of the paleo-Altun and paleo-Kunlun ocean in the south of Tarim was converted to an active continental margin in the Middle Ordovician, experiencing strong compression from south to north and forming a large-scale Middle Caledonian thrust belt [45, 55, 56]. Ordovician carbonate successions were exposed and partially eroded due to uplift related to the Caledonian and Hercynian orogenies (Ordovician–Permian), generating a series of unconformities and/or disconformities (Figure 2), and pervasive karst events directly related to hiatuses [25, 57]. Following closure of the paleo-Altun, paleo-Kunlun, and paleo-Tianshan oceans in the Late Hercynian, Tarim turned into intracontinental basins in the Indosinian and experienced continuous deposition and burial. The Indonesian–Yanshanian (Triassic–Cretaceous) was characterized by intensive faulting in hillside structural belts, whereas in the Himalayan (Cenozoic), faulting concentrated in the foreland basin, closely related to intensive uplift, thrusting, strike-slip thrust, or thrust strike-slip of surrounding orogenic belts [51, 58]. The basin has experienced a period of rapid burial since 5 Ma [51].

The Tabei Uplift in the northern Tarim Basin (Figure 1) comprises a series of Sinian–Devonian marine, Carboniferous–Permian marine–terrestrial, and Triassic–Quaternary terrestrial sedimentary rocks [25, 59] (Figure 2). Hydrocarbon reservoirs are mainly distributed in Ordovician carbonate rocks. During this time, platform margins extended for more than 3000 km, migrating intermittently and producing complex sequence architectures due to the interaction of basin tectonism, topography development, and sea level change [59]. The Halahatang oilfield (Figure 3(a)) is located in the Halahatang Depression, and it is bordered by the Luntai Uplift to the north, the Shuntuoguole Low Uplift to the south, the Lunnan Low Uplift to the east, and the Yingmaili Low Uplift to the west [60–62]. Other important oilfields in the Tabei Uplift include Tahe and Lunnan oilfields to the east [57, 63]. In the Halahatang oilfield, the Ordovician system comprises the Middle–Lower Ordovician Yingshan

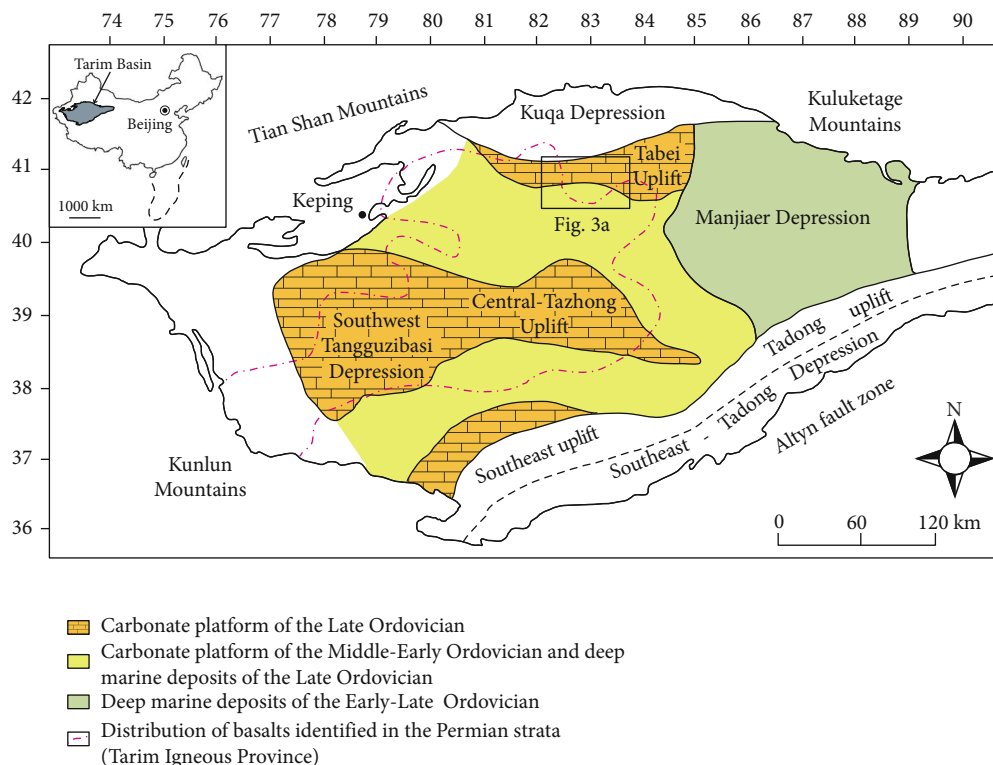


FIGURE 1: Simplified tectonic map of the Tarim Basin showing paleouplifts and depressions (after Zhao et al. [25]), the distribution of platform margins of Ordovician carbonates (after Lin et al. [59]), and occurrence of basalts of the Tarim Large Igneous Province (after Xu et al. [47]).

Formation (O_{1-2y}), Middle Ordovician Yijianfang Formation (O_{2y}), and Upper Ordovician Tumuxiuke (O_{3t}) and Lianglitage (O_{3l}) Formations (Figure 2). Lower-Middle Ordovician carbonate reservoirs are highly heterogeneous, with a caprock of compact muddy limestone and mudstone stratum of the Upper Ordovician Tumuxiuke, Lianglitage, and Sangtamu Formations [25, 57].

3. Materials and Methods

We collected 227 samples of the Yingshan, Yijianfang, Tumuxiuke, and Lianglitage Formations from 16 cores across the study area (Figure 3(b)). Of these, 262 billets were selected for petrographic analysis by standard optical microscopy, with emphasis on the Yijianfang Formation. Thin sections were half stained with Alizarin Red S and potassium ferricyanide in order to facilitate the identification of ferroan and nonferroan calcite, as well as dolomite [64].

Forty thin sections were examined under cathodoluminescence microscopy (optical-CL) using a Reliotron III Cathodoluminescence attachment operated at 10–18 kV gun potential and 0.5–0.6 V beam current. Textural characteristics of limestones and diagenetic cements were investigated using a Zeiss Sigma high-vacuum field emission scanning electron microscope (HV FE-SEM). Carbon-coated samples (~ 15 nm) were imaged under SEM-CL with a Gatan MonoCL4 detector operated at 5 kV and 120 μ m aperture. To investigate the morphology and distribution of nanometer-scale pores, we followed the sample preparation protocol described by

Loucks et al. [65]. We prepared 10×10 mm cubes in 8 samples using the standard X-sectional argon ion milling methods [66]. Samples were then coated with 5 nm of iridium and analyzed using a FEI Nova Nano 430 FE-SEM. Operating conditions were 10–15 kV, spot size of 3–5 nm, and aperture of 30 μ m.

Host rocks and fracture- and vug-filling calcite cements for which enough sample (60 ± 10 μ g of powder) could be obtained with a 500 μ m-thick dental drill were analyzed for C-O (125 samples) and Sr isotopes (21 samples) (Supplementary Materials I and II). Aliquots of ~ 0.3 mg were analyzed for $\delta^{13}C$ and $\delta^{18}O$ using Thermo Fisher Scientific GasBench II coupled to a Thermo Fisher Scientific MAT 253 Isotope Ratio Mass Spectrometer [67, 68]. Samples were reacted in helium-flushed vials with 103% H_3PO_4 at 50°C for 3 hours. Data were calibrated using calcite standards NBS-18 ($\delta^{18}O_{VPDB} = -23.0\text{‰}$, $\delta^{13}C_{VPDB} = -5.0\text{‰}$) and NBS-19 ($\delta^{18}O_{VPDB} = -2.3\text{‰}$, $\delta^{13}C_{VPDB} = 1.95\text{‰}$). Twelve replicates of an internal carbonate standard were analyzed throughout the analytical session to account for analytical drift and precision, reaching an analytical precision of $\pm 0.06\text{‰}$ for $\delta^{13}C_{VPDB}$ and $\pm 0.10\text{‰}$ for $\delta^{18}O_{VPDB}$ routinely.

Carbonate samples were leached in 0.2 M ammonium acetate with a pH of 8 prior to acid digestion for Sr isotopic analysis. Calcite was digested in 4% acetic acid for 10 minutes and dolomite in 8% acetic acid for 15 minutes. Sr was separated in 3 M HNO_3 using Eichrom Sr Specific resin in 70 μ l columns. The total procedure blank for Sr samples was $1 < 30$ pg. Sr samples were loaded onto single

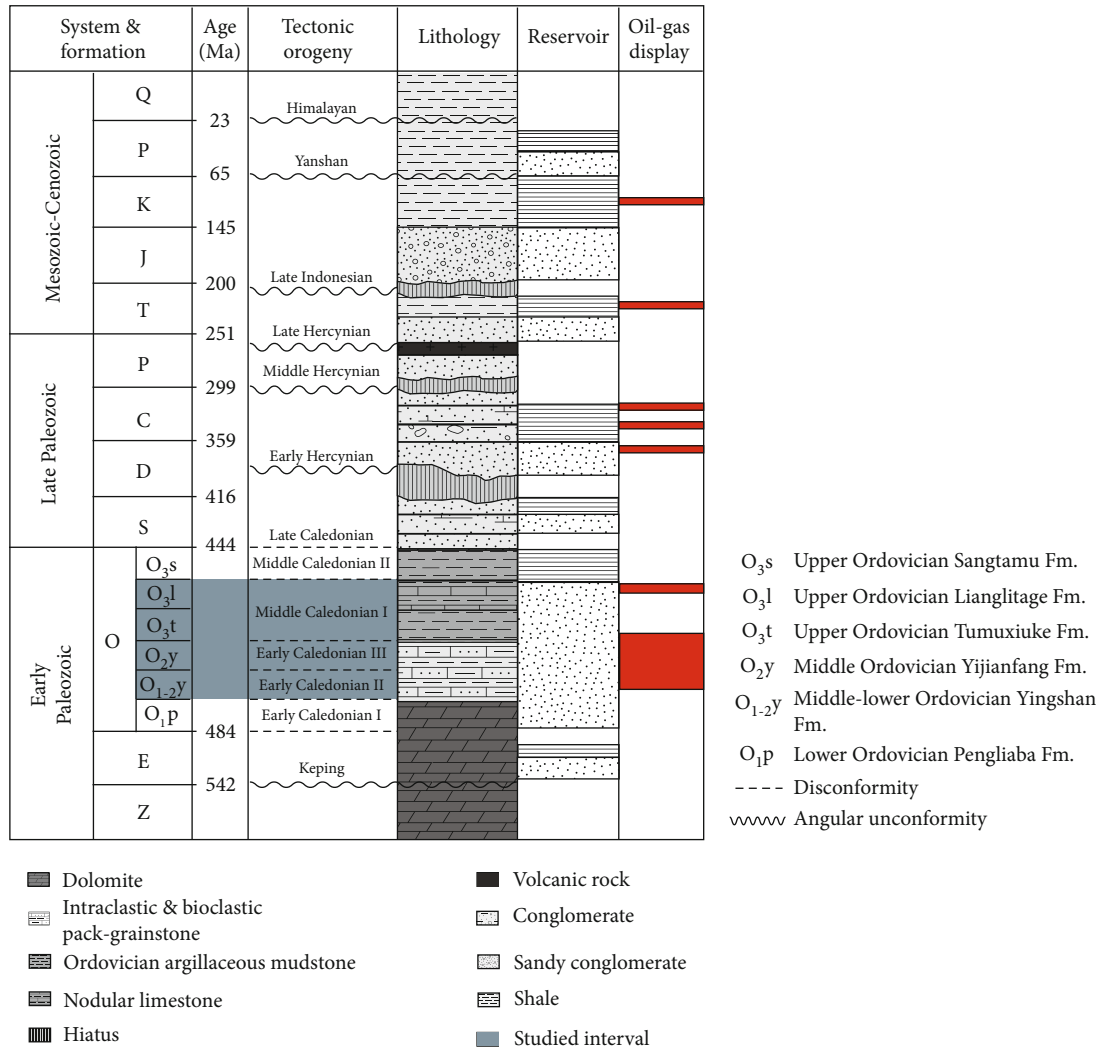


FIGURE 2: Stratigraphy and lithology of Paleozoic-Cenozoic sediments in the Tarim Basin, showing main unconformities and tectonic orogenies (modified from Chang et al. [57] and Zhao et al. [25]).

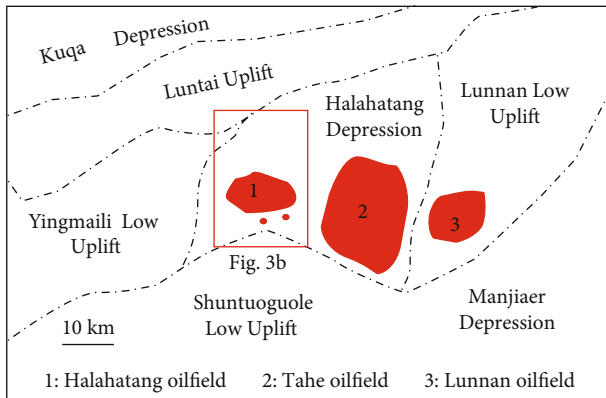
Re filaments with tantalum fluoride and 0.05 M phosphoric acid and subsequently analyzed on a Thermo Fisher Triton thermal ionization mass spectrometer in a static mode. Intensity of ^{87}Sr of 8 V (using 10 – 11 ohm resistors) $\pm 5\%$ was maintained for 8 blocks of 20 cycles with 8-second integration time. The $^{87}\text{Sr}/^{86}\text{Sr}$ ratio was corrected for mass fractionation using $^{87}\text{Sr}/^{86}\text{Sr} = 8.375209$ and an exponential law.

Fluid inclusion microthermometry of 20 doubly polished thin sections was conducted using a gas flow heating-freezing stage (FLUID, Inc.-adapted, U.S. Geological Survey-type) mounted on an Olympus BX-51 microscope. The stage was calibrated using CO_2 ice melting and H_2O ice melting and the critical homogenization temperature of synthetic fluid inclusions [69]. Fluid inclusion petrography and microthermometry followed the procedures of Fall and Bodnar [70]. Liquid-vapor homogenization temperatures (T_h) were determined to be $\pm 1.0^\circ\text{C}$ by thermal cycling using temperature steps of 0.5°C [71] (Supplementary Material III).

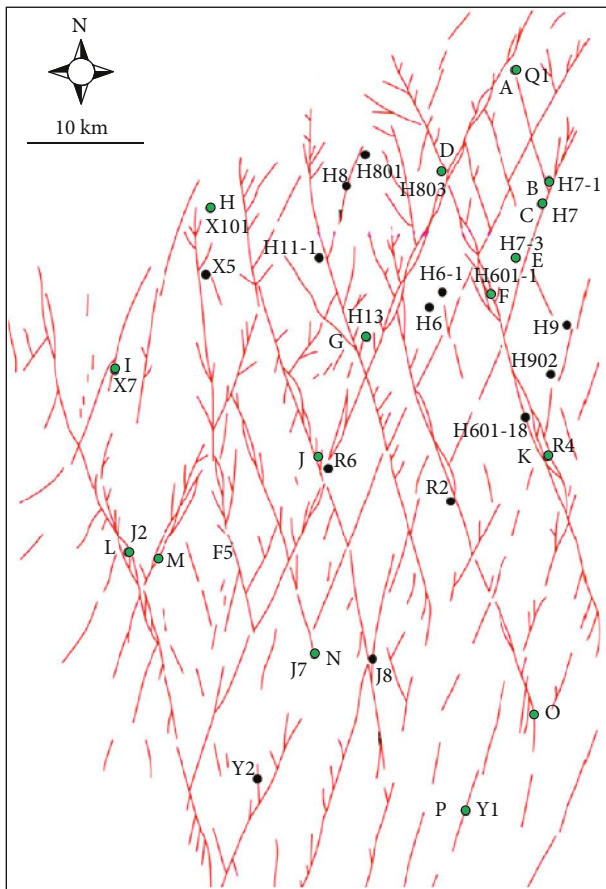
4. Results

4.1. Petrography

4.1.1. Host Rocks. The upper Yingshan and Yijianfang Formations in our study area consist of intraclast packstones and grainstones (Figure 4(a)). These facies are best developed in the northern part of the study area (Figure 3(b), A through I wells), and albeit less abundant, they are also common in the southern part (Figure 3(b), J through P wells). These lithofacies indicate deposition in shallow water with high-energy environment within a wave-dominated shelf. The Tumuxiuke Formation is mud-dominated, mainly composed of bioclast wackestones and peloid wackestones (Figure 4(b)), suggesting that the depositional setting was relatively low energy and deeper marine water during a transgressive period. The basal part of the Lianglitage Formation mostly consists of ooid grains and bioclast grainstones (Figure 4(c)), indicating that the basal part might have been deposited as ooid shoals or bioclast shoals. Upwards, the Lianglitage Formation changes



(a)



(b)

FIGURE 3: (a) Main oilfields in the Halahatang Depression and Lunnan Uplift (from Chang et al. [63]). Red square shows the area studied in cores. (b) Main fault traces in the Halahatang area (after Wu et al. [36]) and location of the studied cores (green dots).

into peloid intraclast packstone and/or bioclast wackestone, and peloid wackestone is also locally present, indicating a low- to moderate-energy depositional environment. The upper intervals contain more fine-grained siliciclastic sedi-

ments, indicating the incorporation of terrigenous sediments into the carbonate system.

Grainstones, packstones, and wackestones of all formations contain little primary porosity, mostly in the form of intraparticle and intercrystalline pores < 150 μm in diameter (Figure 4(c)). Intraparticle pores mostly occur within skeletal fragments such as echinoderms and bryozoans. In the Lianglitage Formation, intraparticle pores are most abundant and localized in a grainstone interval, where they are completely filled with bitumen (Figure 4(c)). Interparticle microporosity is negligible in unaltered host rock.

Interparticle porosity is filled with fibrous to bladed rim (Cc0a), drusy mosaic (Cc0b), and syntaxial calcite cements (Cc0c) (Table 1). Cc0a cement rims are generally <10 μm thick and commonly form the first generation of cement in grainstones and grain-dominated packstones (Figure 4(d)). Cc0b vary from fine to coarsely crystalline (50 to 250 μm) and occur primarily in intraparticle and interparticle pores. Cc0c overgrowth cements are generally 250 μm to 1 mm in size and are common in echinoderm-dominant bioclast grainstone and packstone (Figure 4(e)). Under optical-CL, Cc0a and Cc0b show dull red luminescence (Figure 4(d)), whereas Cc0c shows nonluminescence to bright orange zoned luminescence (Figure 4(e)).

4.1.2. Karstic Features. Clear-cut karstic breccias that contain external sediment were only observed in the Lianglitage Formation. Karstic breccias include crackle breccia, mosaic breccia, clast-supported chaotic breccia, and matrix-rich clast-supported chaotic breccia (Figure 4(f)). Most breccia clasts have a similar lithology, are light red in color, range from very fine to very coarse pebbles in size, and are subangular to subrounded in shape (Figure 4(g)). The matrix is commonly dark brown to reddish brown and contains silt quartz, clays, and iron oxides in sharp contact with clasts (Figure 4(h)).

4.1.3. Mottle Fabrics. A distinctive characteristic of the Yijianfang Formation in the study area are mottle fabrics (term used by Jin et al. (2009) and Fu (2019)), forming dark patches with irregular geometries (single channels or amalgamations of channels with anastomosing geometry) that stand out in core hand samples. Some mottle fabrics are rounded or equant (Figure 5(a)), whereas others are elongated and are herein referred to as channels (Figures 5(b) and 5(c)). Vertical and horizontal elongated channels are localized within the top of the Yijianfang and Tumuxiuke Formations. Mottle fabrics are best developed in the northern part of the study area (Figure 3(b), A through I wells).

Rounded mottle fabrics in the Yijianfang Formation comprise internal, orange to red luminescent, argillaceous carbonate-rich silt (Cs0a) < 20 μm in size (Figure 5(d)). Primary (<3%) and secondary (see below) intergranular micropores and nanopores within mottle fabrics comprise as much as ~10% of the volume of the rock. Most pores are less than 20 μm in size, contain up to 3% illite, and are lined or filled with bitumen (Figures 5(e) and 5(f)). In contrast, vertical and horizontal channels are filled with various mixtures of fragmented fossils and dark-brown calcite mudstone matrix, containing intergrown illite/chlorite, quartz, and phosphates

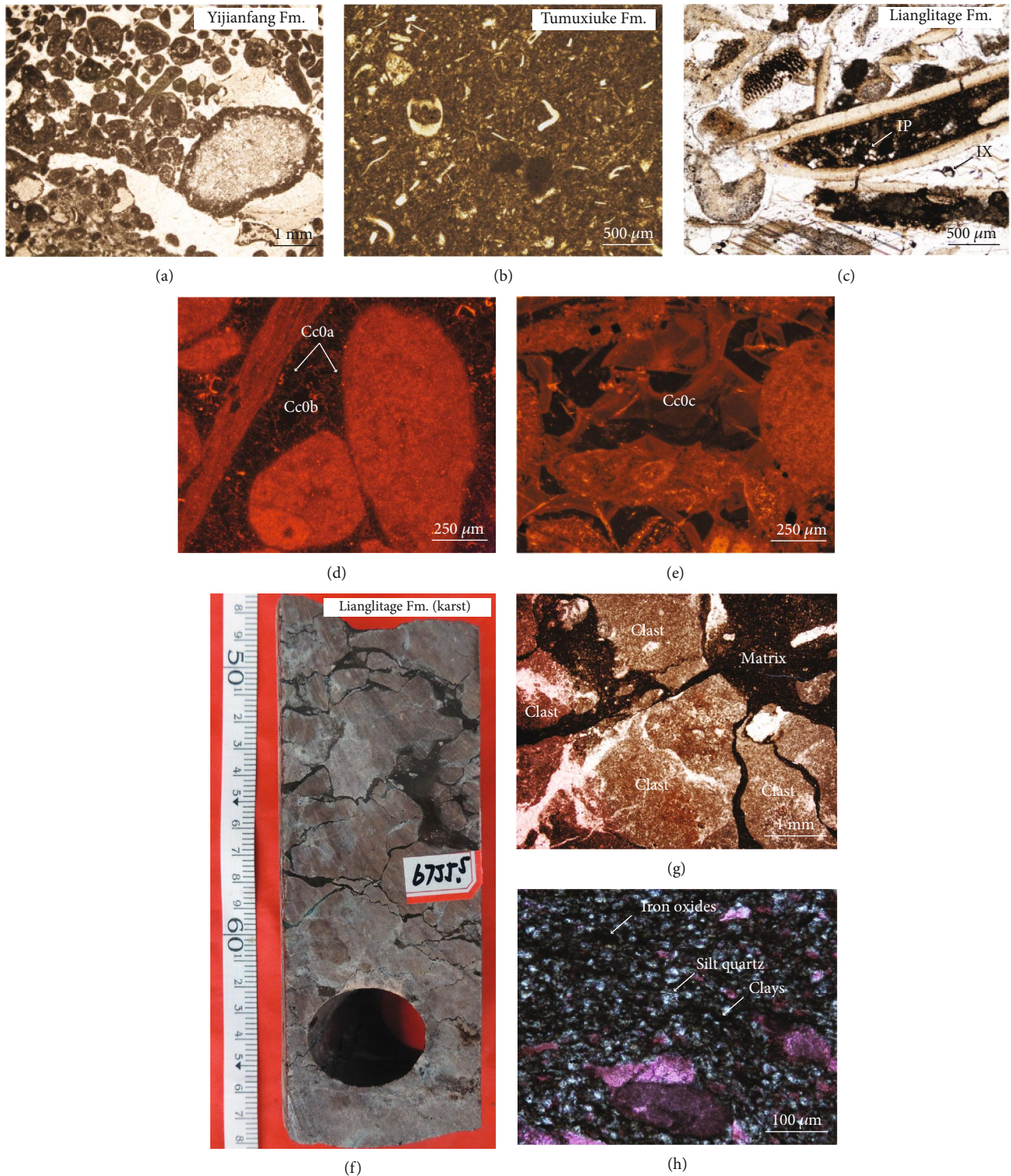


FIGURE 4: Photomicrographs of Ordovician carbonates. (a) Plane light optical photomicrograph of the Yijianfang Formation, (b) Tumuxiuke Formation, and (c) Lianglitage Formation host rocks. IP = interparticle pores; IX = intercrystalline pores. (d) Optical-CL photomicrograph of grainstone cemented by fibrous to bladed calcite rims (Cc0a) and drusy mosaic (Cc0b) cements. (e) Optical-CL photomicrograph of grainstone cemented by syntaxial cement (Cc0c). (f) Hand specimen of the karstic horizon within the Lianglitage Formation showing matrix-rich, clast-supported chaotic breccia. (g) Plane light optical photomicrograph of angular red clasts in Lianglitage Formation breccias. (h) Close-up photomicrograph of the breccia matrix.

TABLE 1: Summary of petrographic characteristics of the main diagenetic features and cements shown in chronological order (paragenetic sequence). KB: matrix karstic breccia; F: fracture; V: dissolution vug; S: stylolite; Cc: calcite cement; Cs: calcite sediment; Dc: dolomite cement.

Feature	Cement	Formation	Morphology	Crystal size	CL	SEM-CL
Host rock	–	Yingshan	micrite	< 4 mm	Orange to dull red	Light-luminescent; slightly zoned
		Yijianfang	micrite			
		Tumuxiuke	micrite			
		Lianglitage	micrite			
Host rock cementation	Cc0a	Yingshan; Yijianfang; Tumuxiuke; Lianglitage	rim	< 10 mm	Dull red	Light-luminescent; slightly zoned
	Cc0b	Yingshan; Yijianfang; Tumuxiuke; Lianglitage	drusy	50 to 250 mm	Dull red	Dark- to light luminescent; zoned
	Cc0c	Yingshan; Yijianfang; Tumuxiuke; Lianglitage	syntaxial	250 mm to 1 mm	Non-luminescent to bright orange zoned	Light-luminescent; slightly zoned
Dark mottles	Cs0a	Yingshan; Yijianfang; Tumuxiuke;	silt	< 20 mm	Orange to dull red	Light-luminescent; slightly zoned
	Cs0b	Top Yijianfang; Tumuxiuke	mud	< 4 mm	Orange to dull red	Light-luminescent; slightly zoned
F1	Cc1	Yijianfang; Tumuxiuke;	pallisade	300 mm - 1 mm	Non-luminescent to bright orange zoned	Light-luminescent; slightly zoned
	Cs1	Yijianfang; Tumuxiuke;	silt	10-75 mm	Non-luminescent	–
Karstic breccias	KB	Lianglitage	silt	250 mm to 2 mm	–	–
V2						
F2a	Cc2	Yingshan; Yijianfang; Tumuxiuke; Lianglitage	blocky	50 - 250 mm	Non-luminescent to bright orange zoned	Dark- to light luminescent; zoned
F2b						
S1a & S1b	–	Yingshan; Yijianfang; Tumuxiuke; Lianglitage	–	–	–	–
F3a	Cc3a	Yingshan; Yijianfang; Tumuxiuke; Lianglitage	rim	50 - 200 mm	Dark red to bright orange luminescent	Dark- to light-luminescent; zoned
F3b						
F3c	Bitumen	–	–	–	–	–
V3	Cc3b	Lianglitage	blocky	500 mm - 2 mm	Orange luminescent	Light-luminescent; unzoned
F4a						
F4b	Cc4	Yijianfang; Tumuxiuke	blocky	50 mm - 1 mm	Red luminescent	Dark-luminescent; unzoned
V4						
F5	Fluorite	Yijianfang	euhedral	up to 5 cm	–	–
	Barite	Yijianfang	euhedral	up to 4 mm	–	–
	Cc5	Yijianfang	blocky	200 - 250 mm	Red to dull red luminescent	Light-luminescent; slightly zoned
	Recrystallized host rock	Yingshan; Yijianfang	crystalline	< 4 to 50 mm	Red to dull red luminescent	Light-luminescent; slightly zoned
F6	Cc6	Yingshan; Yijianfang	blocky	200 - 600 mm	Dull red to non-luminescent	Light luminescent; unzoned
V6						
F7a	Cc7a	Yingshan; Yijianfang; Tumuxiuke; Lianglitage	bridges	50 - 100 mm	–	Light-luminescent; unzoned
F7b	Cc7b	Yingshan; Yijianfang; Tumuxiuke; Lianglitage	blocky	50 mm - 1 mm	–	Light-luminescent; unzoned
V7						
F7c & S2	Dc1	Yingshan; Yijianfang; Tumuxiuke; Lianglitage	euhedral	< 30 mm	–	Dark-luminescent

(Cs0b) (Figures 5(g) and 5(h)). Intergranular micropores in channels constitute <10–15% of the volume of the channel and are partially infilled with 5–10% illite, kaolinite, and bitumen (Figure 5(i)).

Ordovician host rocks, including mottle fabrics, are crosscut by several types and generations of partially to fully cemented fractures, stylolites, and dissolution vugs (Table 1). The classification below was established for the Yijianfang Formation, but on the basis of textural and geochemical similarities, we extend this classification to similar features present in the Yingshan, Tumuxiuke, and Lianglitage Formations.

4.1.4. Fractures. On the basis of crosscutting relationships and the type of cement fill, we define seven groups of opening-mode fractures, from oldest (F1) to youngest (F7) (Table 1). Bed-perpendicular and bed-oblique calcite-filled fractures (F1) with irregular walls and apertures between 0.5 and 1 cm occur mostly in the uppermost part of the Yijianfang and Tumuxiuke Formations (Figure 6(a)). Calcite cement fill (Cc1) in these fractures consists of equant to bladed subhedral crystals grading rapidly to palisade morphology. Palisade calcite crystals are 300 μm to 1 mm long and 10–50 μm wide and can develop up to 3 cm thickness (Figure 6(b)). Crystals are slightly curved and show undulatory extinction. Under SEM-CL, they are light luminescent and slightly zoned. Former remnant open porosity in F1 fractures is filled with internal yellow sediment (Cs1) composed of blocky calcite 10 to 75 μm in size and clay minerals (Figure 6(b)).

The second group of fractures (F2) includes bed-perpendicular and bed-oblique calcite-filled microfractures (<0.5 mm in aperture) with straight to irregular (sigmoidal) walls (F2a) (Figure 6(c)) and planar, subhorizontal calcite-filled fractures (F2b) with apertures ranging from 100 μm to 4 mm (Figure 6(d)). F2 fractures are present in the Yingshan, Yijianfang, Tumuxiuke, and Lianglitage Formations. F2 fractures are filled with blocky, zoned, nonluminescent to bright orange calcite crystals (Cc2) ranging between 50 and 250 μm in diameter (Figure 6(e)). Micron-sized (5–20 μm) bright orange Cc2 calcite overgrowths overlap Cs0a calcite sediment (Figure 5(d)).

F3 fractures are present within the Yingshan and Yijianfang Formations and to a lesser extent in the Tumuxiuke and Lianglitage Formations. This group includes bed-perpendicular and bed-oblique calcite- and bitumen-filled fractures with straight walls and apertures of 100–500 μm (F3a in Figure 6(f)), slightly wider (500 μm –1 cm) fractures of similar characteristics that may preserve partially open porosity (F3b in Figure 6(f)), and planar bitumen-filled microfractures with apertures < 100 μm (F3c). Calcite cements in F3 fractures are zoned, dark red to bright orange in luminescence, bladed to blocky rim cements, and 50 to 200 μm in size, with euhedral terminations (Cc3a) (Figures 6(g)–6(i)). Some F3 fractures preserved partial porosity that was subsequently infilled by bitumen (Figures 6(g)–6(i)).

The fourth group of fractures (F4) is common in the Yijianfang Formation and less abundant in the Tumuxiuke and Lianglitage Formations. This group encompasses planar bed-perpendicular and bed-oblique fractures rang-

ing between 0.5 mm and 2 cm in aperture with irregular margins and calcite+bitumen±minor late pyrite cement (F4a in Figures 6(j) and 6(l)) and vertical microfractures that terminate ~1 cm away from horizontal stylolites and are subparallel to stylolite teeth (F4b in Figure 6(k)). F4 fractures are filled with blocky calcite crystals, 50 μm to 1 mm in diameter, which show red luminescence (Cc4 in Figures 6(k)–6(l)).

Fractures in the fifth group (F5) are only present in the Yingshan and Yijianfang Formations. F5 fractures are bed-perpendicular and/or bed-oblique to bedding and have irregular walls and apertures between 1 mm and >7 cm (Figure 7(a)). F5 fractures are filled with euhedral fluorite, barite, and calcite cement (Cc5), up to 5 cm in size, in variable proportions (Figure 7(b)), and are associated with calcite and celestite host rock replacement in cores L, N, and K (Figure 3(b)). Calcite and celestite mineralization is nonpenetrative and limited to a few millimeters to centimeters away from F5 fracture walls. Pores around celestite crystals are commonly less than 100 μm in size (Figure 7(c)). In most cases, fluorite and barite predate calcite cementation (Figures 7(a) and 7(b)), and although textures are ambiguous, celestite replacement appears to be closely related to fluorite and barite mineralization. In a few examples, barite and fluorite appear to be coeval, whereas in others, fluorite was followed by calcite and finally barite precipitation. Cc5 in F5 fractures is blocky, 200 to 250 μm in size, and shows red to dull red luminescence (Figure 7(b)). Silica mineralization (microcrystalline quartzchert) occurs along some F5 fracture walls (Figure 7(a)). Within silicified areas, pores of various shapes are as much as 400 μm long (Figure 7(d)).

F6 fractures are bed-perpendicular, bed-oblique, and/or bed-parallel calcite-filled fractures with irregular walls and apertures between 1 mm and 3 cm (Figure 7(e)). Blocky calcite cement (Cc6) in F6 fractures ranges between 200 and 600 μm in size (Figure 7(f)), is dull red to nonluminescent, and appears unzoned under SEM-CL.

F7 fractures are present in all formations. This group comprises bed-perpendicular and bed-oblique calcite-filled fractures ranging between 50 μm and 2 mm in aperture (F7a in Figures 7(g) and 7(h)), tension gashes (F7b in Figure 7(i)) associated with stylolites oriented at an angle to bedding (S2, see below), and bedding-oblique to bedding-perpendicular stylolitic and sheared fractures (F7c in Figure 7(j)). F7a fractures are filled with calcite cement forming bridges that span across fracture walls Cc7a in Figure 7(h). Bridges are evidenced by fracture wall-parallel trails of fluid inclusions (see below) indicating a crack-seal mechanism of cementation during fracture opening (synkinematic cement; discussed by Lander and Laubach [72] and Ukar and Laubach [73]). Bridges are not remnants of dissolved calcite but indicate calcite accumulation that depends on thermal exposure and renewal of the fracture surface area during repeated fracture opening [72]. F7a fractures may preserve as much as 25% residual porosity. Tension gashes (F7b) tip out ~1 cm away from S2 stylolites and are subparallel to stylolite teeth (Figure 7(i)). F7b fractures are filled with blocky calcite cement (Cc7b) and dolomite cement (Dc1) (Figure 7(i)). Cc7b ranges between 50 μm and 1 mm in size and appears unzoned and light luminescent under SEM-CL. Dc1 forms

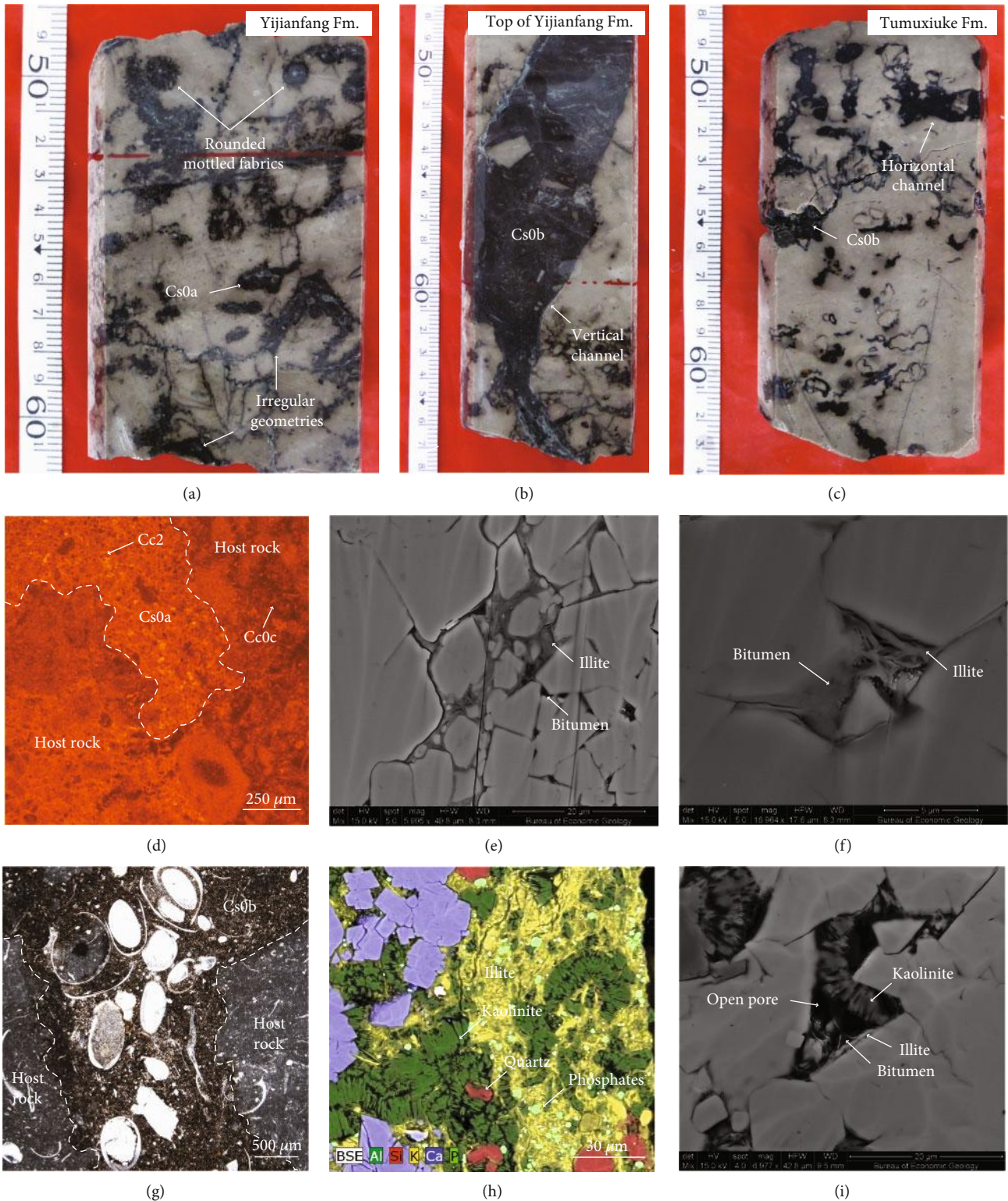


FIGURE 5: Hand specimen of middle Yijianfang Formation (a), top of the Yijianfang Formation (b), and Tumuxiuke Formation (c) showing rounded and elongated mottle fabrics (channels) filled with calcite sediment Cs0. (d) Optical-CL photomicrograph of packstone showing subrounded mottle fabrics filled with calcite sediment Cs0a subsequently cemented by Cc2. (e, f) SEM images showing carbonate-rich detritus Cs0a within mottle fabrics. Most of the interparticle porosity is filled with illite and/or bitumen (f). (g) Plane light optical photomicrograph of wackestone showing vertical channels filled with calcite sediment Cs0b. (h, i) SEM images showing carbonate-rich detritus Cs0b within vertical channels. Most of the interparticle porosity is filled with illite, kaolinite, and/or bitumen (i).

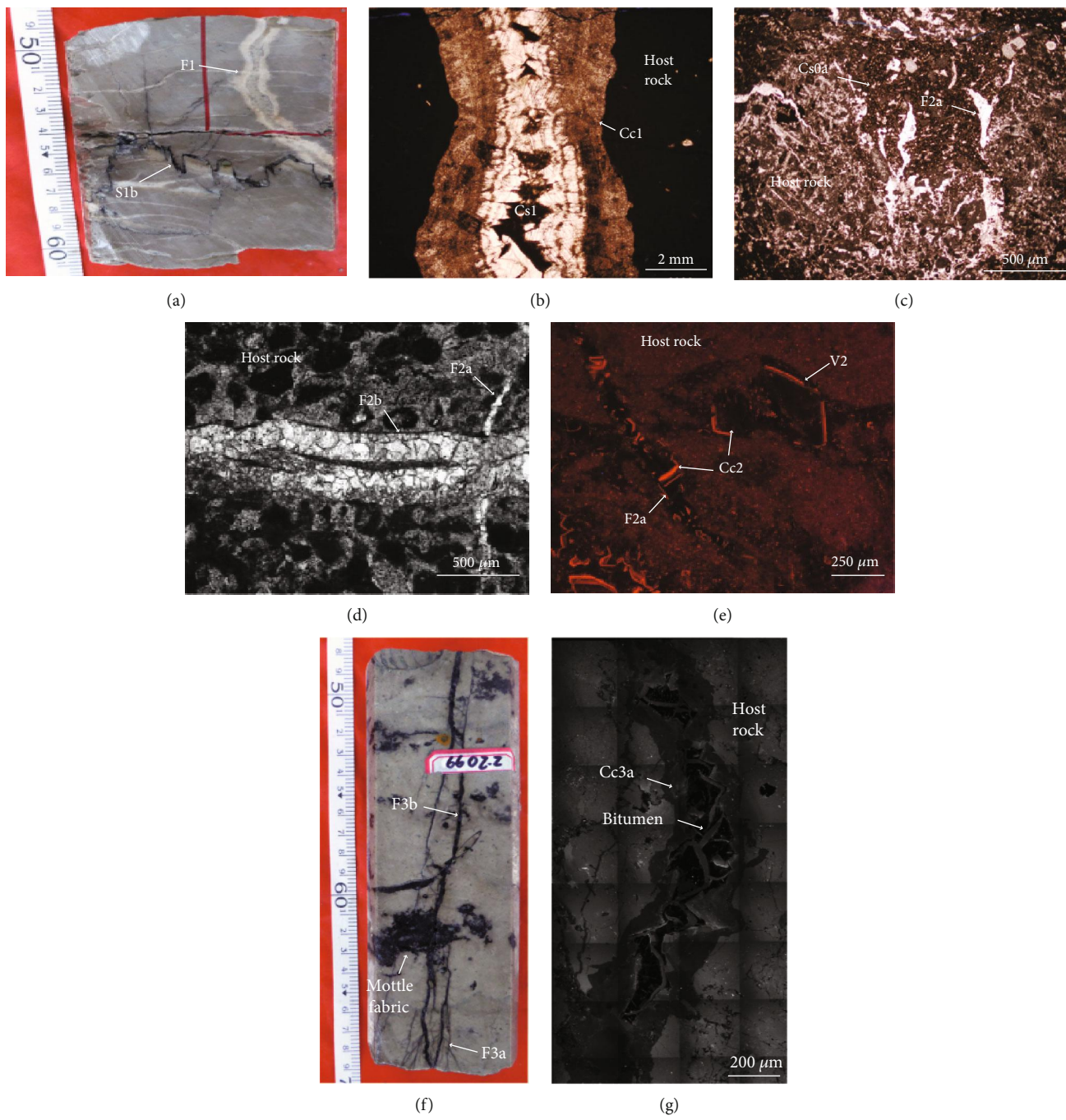


FIGURE 6: Continued.

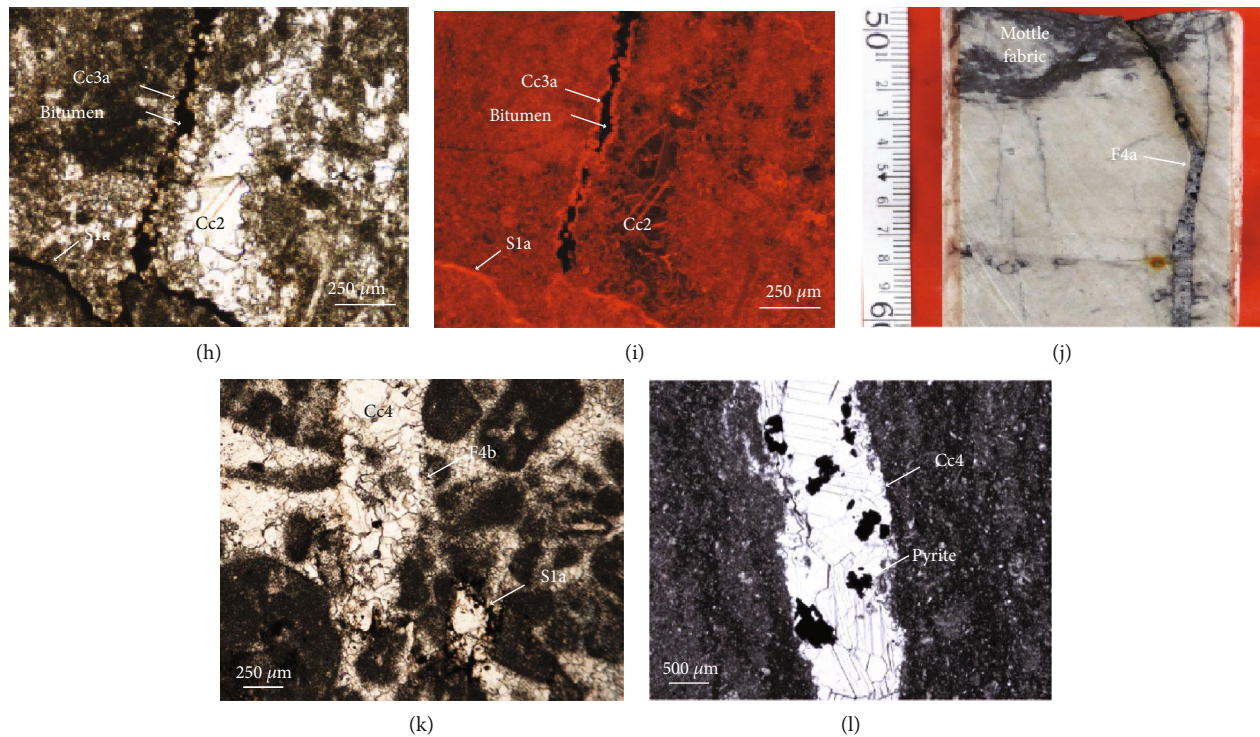


FIGURE 6: (a) Hand specimen of the Tumuxiuke Formation showing F1 fractures. (b) Plane light optical photomicrograph of palisade calcite (Cc1) and internal sediment (Cs1) in an F1 fracture. (c) Plane light optical photomicrograph of F2a fractures crosscutting calcite sediment Cs0a within rounded mottle fabrics. (d) Plane light optical photomicrograph showing a F2b fracture crosscutting a F2a fracture. (e) Optical-CL photomicrograph showing Cc2 calcite infilling F2 fractures and V2 vugs. (f) Hand specimen of the Tumuxiuke Formation showing F3 fractures. F3 fractures cross-cut rounded mottle fabrics. (g) Panchromatic SEM-CL image showing Cc3a calcite crystals that are zoned in SEM-CL. Bitumen fills remaining void space in the center of the fracture. (h, i) Cc2 and Cc3a calcite cements under (h) plane light and (i) optical-CL. (j) Hand sample specimen showing F4a fractures. (k) Plane light optical photomicrograph showing F4b fractures filled with blocky calcite (Cc4). (l) Plane light optical photomicrograph showing F4a fractures filled with blocky calcite (Cc4) and concurrent pyrite.

isolated, subhedral to euhedral, dark luminescent crystals up to $30\ \mu\text{m}$ in diameter. Pores around Dc1 crystals are as much as $100\ \mu\text{m}$ in size (Figure 7(i)). F7c fractures contain insoluble residual material, bitumen, and Cc7b and Dc1 cements (Figure 7(j)).

4.1.5. Stylolites. Bed-parallel stylolites (S1a) and solution seams (S1b) are ubiquitous and abundant in all formations and cores studied. S1a stylolites occur mainly in intraclast packstones and grainstones from the Yingshan, Yijianfang, and lower Lianglitage Formations. S1a contain intergrown illite/chlorite, quartz, phosphates, pyrite, kaolinite, and bitumen (Figure 8(a)). S1b solution seams have similar mineralogies with the addition of fine-grained detrital sediments including as much as 20% of illite, intergrown illite/chlorite, and quartz (Figure 8(b)). S1b are present in mud-dominated lithofacies such as bioclast wackestones and peloid wackestones from the Tumuxiuke and upper Lianglitage Formations. S1 are cut by F1 fractures, but some S1 crosscut F3 and F4 fractures indicating that S1 formation was continued in time.

Bed-perpendicular to bed-oblique stylolites (S2) are locally abundant, best developed in J, L, M, N, O, and P cores (Figure 3(b)). Randomly oriented S2 give the rock a pseudo-

nodular appearance described as stylobreccia by Stewart and Hancock [74] (Figures 7(g) and 8(a)). S2 contain dolomite cement (Dc1), calcite cement (Cc7b), insoluble material, and bitumen (Figures 7(i) and 7(j)). S2 stylolites are associated with F7 fractures and crosscut all previous diagenetic features (Figures 7(g) and 7(k)).

4.1.6. Cavities and Vugs. Pores larger than the average grain size ($\sim 20\ \mu\text{m}$) are abundant in host rocks of all formations. Vugs are usually between 0.5 and 2 mm in diameter, although some exceed 1 cm (Figure 8(a)), and have irregular edges supporting dissolution as their formation mechanism. Many vugs are associated with or terminate at fractures, indicating a temporal and genetic relationship among fractures and vugs (Figure 8(a)). Crosscutting relationships between different types of vugs could not be established, but on the basis of the association between fractures and vugs and similarities in mineral fill, we describe five generations of vugs formed synchronously with F2–F7 fractures.

Although textural evidence indicates that mottle fabrics were not open voids in the sense of karstic breccias such as those found in the Lianglitage Formation, mottle fabrics are the earliest dissolution feature in the Yijianfang Formation.

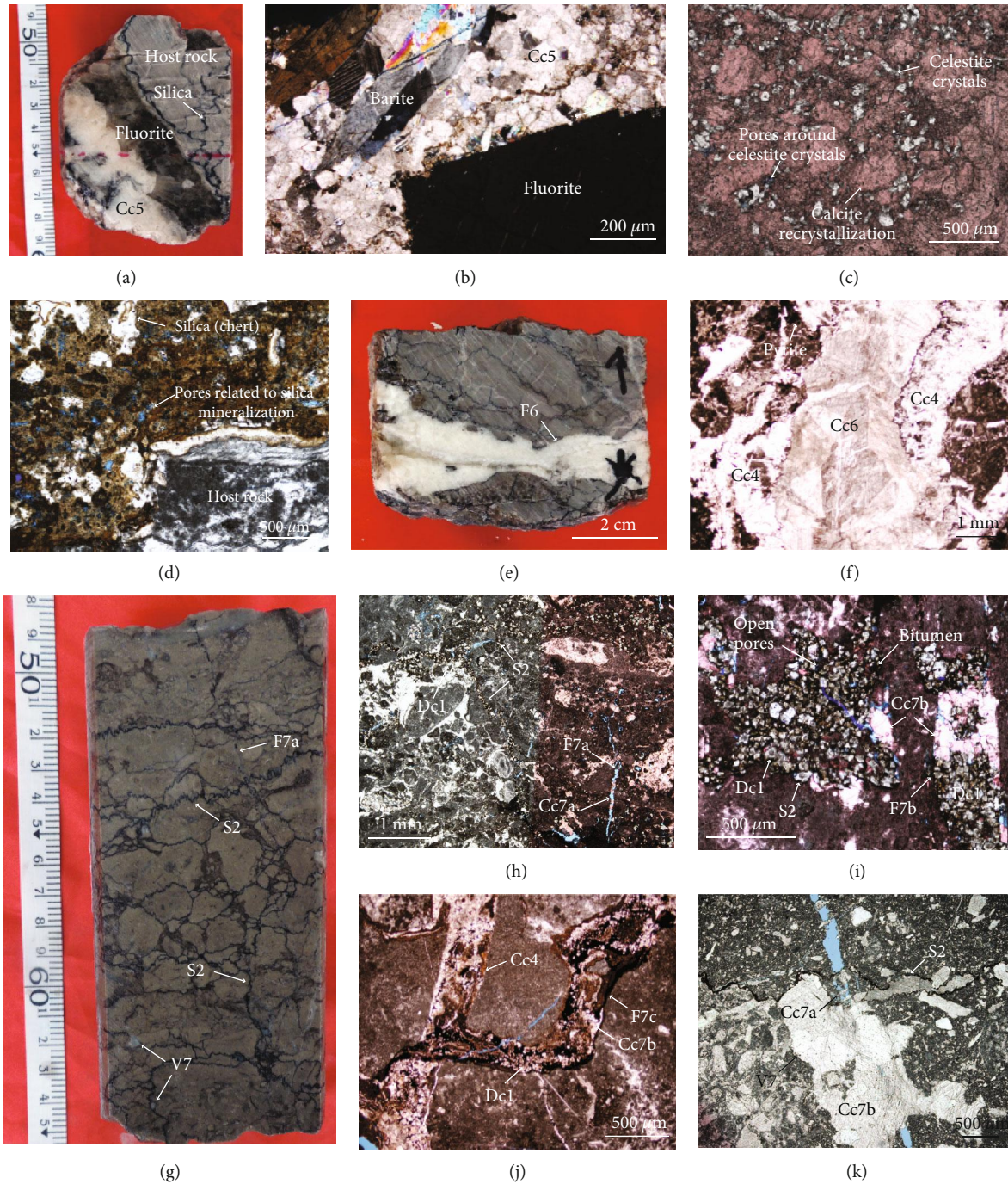
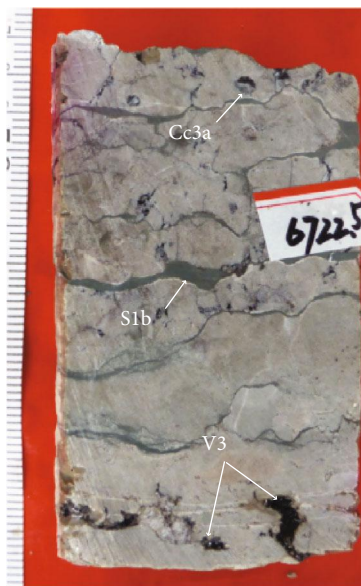


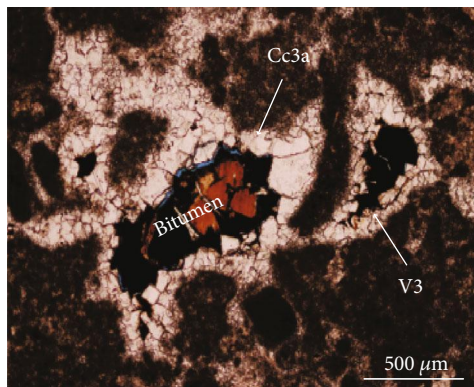
FIGURE 7: (a) Hand specimen of the Lianglitage Formation showing F5 fractures cemented by fluorite and calcite (Cc5). Silica mineralization in the host rock along the fracture wall. (b) Plane light optical photomicrograph showing fluorite, barite, and Cc5a calcite cement precipitated within a F5 fracture. (c) Plane light optical photomicrograph showing recrystallization of host rock by calcite and celestite mineralization. Note pores (filled with blue epoxy) formed around the celestite crystals. (d) Plane-light optical photomicrograph showing partial replacement of the host rock by silica mineralization. Note pores associated with silica replacement. (e) Hand specimen of Yijianfang Formation showing F6 fractures. (f) Plane light optical photomicrograph showing F6 fractures filled with Cc6 cement postdating Cc4-bearing F4 fractures. (g) Hand specimen of the Yijianfang Formation showing irregular, multidirectional S2 stylolites that give the rock a pseudonodular appearance (stylobreccia). Note that S2 is associated with F7 fractures and V7 vugs. (h) Plane light optical photomicrograph showing stylobreccias and their association with F7 fractures. Dolomite cement (Dc1) precipitated along S2 stylolites. F7a fractures filled with calcite cement (Cc7a). (i) Plane light optical photomicrograph showing F7b fractures and S2 tectonic stylolites containing blocky calcite (Cc7b) and dolomite cement (Dc1). Notice that pores around Dc1 crystals are filled with bitumen. (j) Plane light optical photomicrograph showing bedding-oblique stylolitic and sheared F7c fractures containing insoluble material, bitumen, and calcite cement (Cc7b). (k) Plane light optical photomicrograph showing an F7a fracture filled with calcite cement (Cc7a) forming synkinematic bridges and V7 vugs filled with blocky cement (Cc7b).



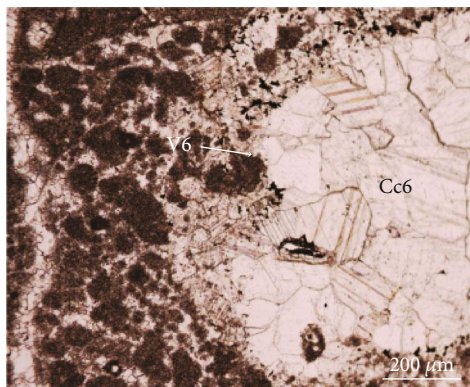
(a)



(b)



(c)



(d)



(e)



(f)

FIGURE 8: Continued.

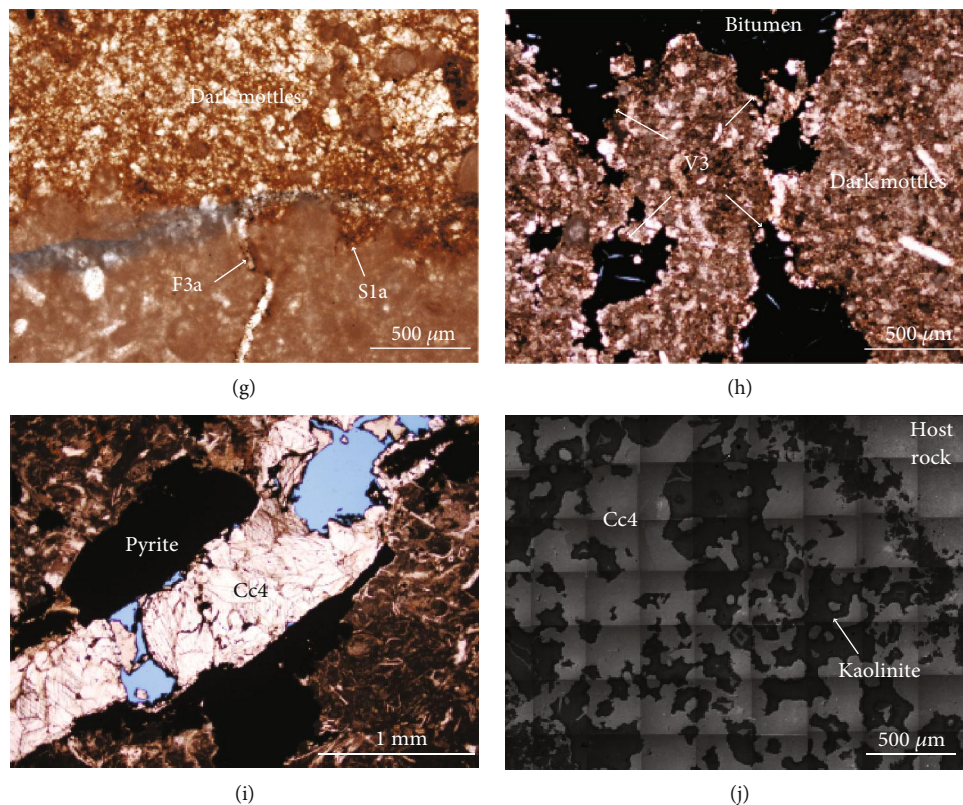


FIGURE 8: (a, b) Hand specimen of the Yijianfang Formation showing S1a, S1b, and S2 stylolites and V3 and V4 dissolution vugs. (c) Plane light optical photomicrograph showing a V3 lined by Cc3a calcite cement and bitumen. (d) Plane light optical photomicrograph showing a V6 vug filled with blocky Cc6. (e, f) Hand specimens and (g) plane light optical photomicrograph of the Yijianfang Formation showing an association between F3a, S1a, and dark mottles. (h) Plane light optical photomicrograph showing V3 vugs occurring within a dark mottle. Bitumen-infilled vugs and interparticle porosity within mottle fabrics. (i) Plane light optical photomicrograph showing pyrite mineralization and an F4a fracture enlarged by secondary dissolution. (j) Panchromatic SEM-CL photomosaic showing corroded Cc4 and precipitation of kaolinite into dissolved voids.

We designate these as the first generation of vugs (V1). V2 vugs overprint mottle fabrics and are infilled with blocky, nonluminescent to bright orange luminescent calcite (Cc2; Figure 6(e)), whereas V3 vugs are partially infilled with bladed to blocky rim cements (Cc3a) and bitumen (Figures 8(b) and 8(c)) and V4 vugs contain red luminescent calcite (Cc4; Figure 8(a)). No V5 vugs were identified in cores. V6 and V7 vugs are infilled with coarse blocky calcite cement (Cc6 and Cc7b, respectively) (Figures 7(k) and 8(d)). V3 are the most abundant type of vug in the Yijianfang Formation and are also present in the Yingshan and Tumuxiuke Formations, within the karstic horizon of the Lianglitage Formation. V3 are present in A–I cores, coinciding with the location of mottle fabrics in the northern part of the study area (Figure 3(b)). In fact, F3, V3, S1, and mottle fabrics show a close relationship (Figures 8(e) and 8(f)); where an F3 and/or S1 encounter a dark mottle, porosity (secondary) increases giving the rock the aspect of pseudobreccia as described by Fu [35]. In some cases, this secondary dissolution affects the area immediately surrounding the mottle fabric (Figure 8(g)). The pore space within mottle fabrics was subsequently infilled with bitumen giving these areas their characteristic dark color (Figure 8(h)).

Cc3b and Cc4 that precipitated in fractures show dissolution corrosion (Figures 8(b) and 8(i)) providing evi-

dence of dissolution-enhanced fractures. Corroded Cc4 calcite is usually associated with metal sulfides (pyrite mineralization) and kaolinite (Figures 8(i) and 8(j)). This dissolution event resulted in the formation of as much as 15% secondary porosity.

4.2. Geochemistry. Stable isotopic and fluid inclusion analyses were conducted in order to shed light on the origin of the fluids that led to the precipitation of fracture- and vug-filling cements. Geochemical analyses are summarized in Table 2 and Supplementary Materials I, II, and III.

4.2.1. Carbon and Oxygen Isotopes. Yingshan and Yijianfang Formation host rocks yielded $\delta^{18}\text{O}$ values ranging from -7.7 to -4.7‰VPDB and $\delta^{13}\text{C}$ values ranging from -0.1 to +1.6‰VPDB (Figure 9). $\delta^{18}\text{O}$ of Tumuxiuke Formation carbonates ranges from -6.7 to -5.9‰VPDB and $\delta^{13}\text{C}$ from -0.6 to +1.7‰VPDB, whereas $\delta^{18}\text{O}$ of Lianglitage Formation carbonates ranges from -8.7 to -4.3‰VPDB and $\delta^{13}\text{C}$ varies from -0.6 to +3.2‰VPDB. Red clasts within Lianglitage karstic breccias have $\delta^{18}\text{O}$ ranging from -7.3 to -6.4‰VPDB and $\delta^{13}\text{C}$ ranging from +1.2 to +1.7‰VPDB (Figure 9).

Cs0 in mottle fabrics in the Yingshan, Yijianfang, and Tumuxiuke Formations have $\delta^{18}\text{O}$ values slightly more

TABLE 2: Summary of geochemical and microthermometric characteristics of the main diagenetic features and cements shown in chronological order (paragenetic sequence). KB: matrix karstic breccia; F: fracture; V: dissolution vug; S: stylolite; Cc: calcite cement; Cs: calcite sediment; Dc: dolomite cement.

Feature	Cement	$\delta^{18}\text{O}$ (VPDB)	$\delta^{13}\text{C}$ (VPDB)	$^{87}\text{Sr}/^{86}\text{Sr}$	Th ($^{\circ}\text{C}$)	Salinity (wt.% eq. NaCl)	Oil inclusions	T oil ($^{\circ}\text{C}$)
Host rock	-	-7.4 to -5.5	-0.1 to 1.1	0.7088	-	-	No	-
		-7.7 to -4.7	-0.3 to 1.6	0.7088 to 0.7089	-	-	No	-
		-6.7 to -5.9	-0.6 to 1.7	0.7089 to 0.7090	-	-	No	-
		-8.7 to -4.3	-0.6 to 3.2	0.70856	-	-	No	-
Host rock cementation	Cc0a	-	-	-	-	-	No	-
	Cc0b	-	-	-	74 to 150	1.4 to 7.7	No	-
	Cc0c	-	-	-	75 to 131	1.6 to 5.6	No	-
Dark mottles	Cs0a	-9.1 to -6.3	-0.5 to 1.1	0.7091	-	-	No	-
	Cs0b	-	-	-	-	-	No	-
F1	Cc1	-7.8 to -3.6	0.3 to 2.1	0.7087	76.9 to 113.9	1.9 to 2.7	No	-
	Cs1	-	-	-	-	-	No	-
Karstic breccias	KB	-	-	0.7099	-	-	No	-
V2								
F2a F2b	Cc2	-9.1 to -4.5	-3.8 to 2.2	-	74 to 135	2.4 to 5.7	No	-
S1a & S1b	-	-	-	-	-	-	-	-
F3a F3b	Cc3a	-11.7 to -7.1	-0.2 to 2.8	0.7085 to 0.7088	60 to 165	0.4 to 12.3	Yellow to dull blue	60 to 75
V3	Cc3b	-12.8 to -9.3	1 to 2	0.7085	50 to 100	7.7 to 14.1	-	-
F4a F4b V4	Cc4	-15.8 to -13.7	-0.4 to 1.7	0.7094 to 0.7102	80 to 96	13.5	Bright blue to green-blue	-
F5	Fluorite	-	-	-	79 to 112	9.6 to 10.5	Yellow-green to green	-
	Barite	-	-	-	117 to 144	11.1 to 19	-	-
	Cc5	-13.7 to -9.7	-2.4 to -2.2	0.7090	61 to 97.8	5.7 to 14.7	-	-
	Recrystallized host rock	-11.1 to -6.4	-1.8 to -0.1	-	-	-	-	-
F6 V6	Cc6	-15.4 to -8.5	-4.8 to -0.2	0.7093 to 0.7094	95 to 123	4.7 to 10.5	-	-
F7a	Cc7a	-	-	-	-	-	Dull blue	44 to 58
F7b V7	Cc7b	-18.3	-1.1	-	-	-	Light blue	-
F7c & S2	Dc1	-	-	-	-	-	-	-

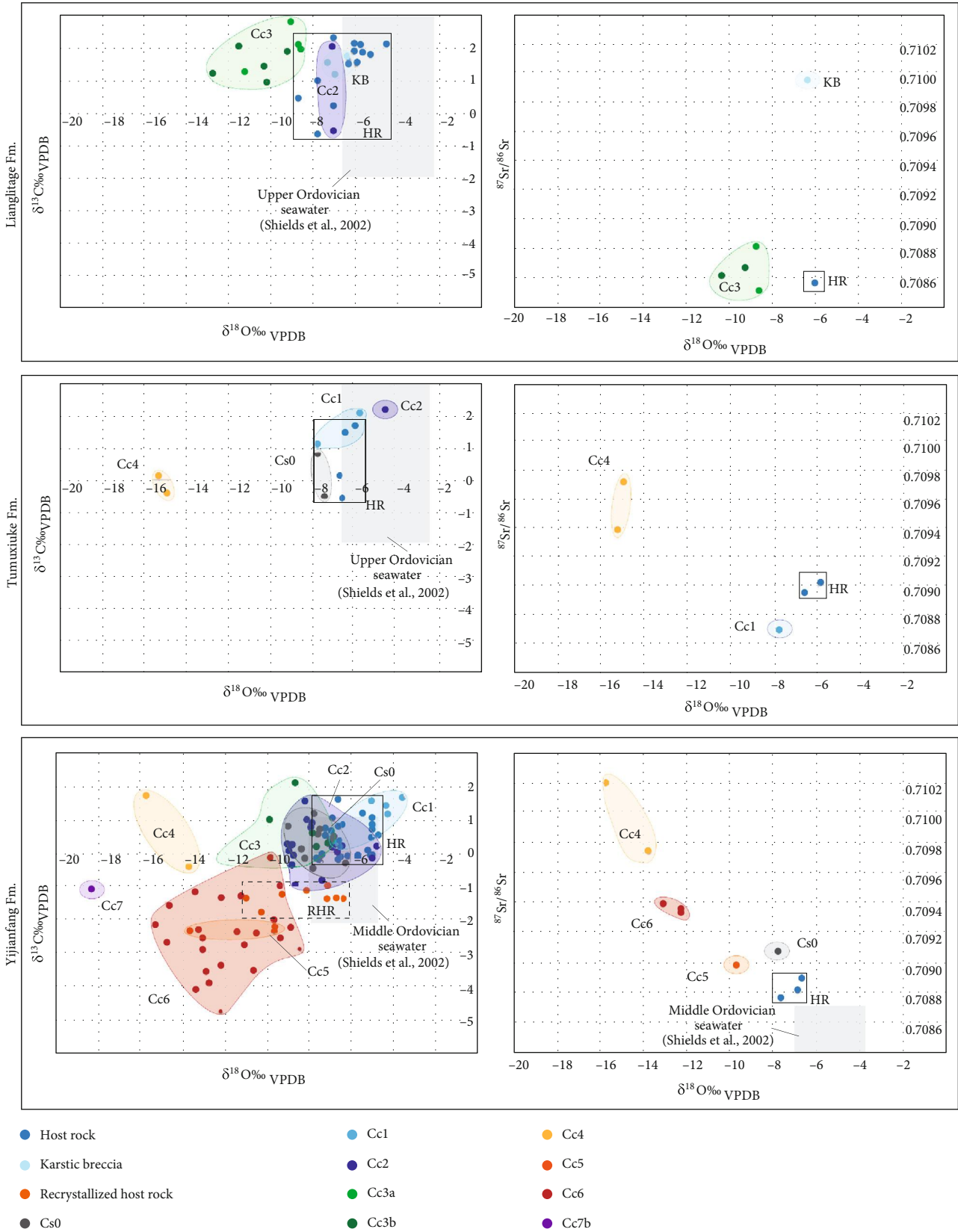


FIGURE 9: $\delta^{18}\text{O}$ - $\delta^{13}\text{C}$ and $^{87}\text{Sr}/^{86}\text{Sr}$ - $\delta^{18}\text{O}$ crossplots arranged by formation. Light grey polygons show $\delta^{18}\text{O}$ - $\delta^{13}\text{C}$ and $^{87}\text{Sr}/^{86}\text{Sr}$ ranges of Middle Ordovician and Upper Ordovician marine carbonates from Shields et al. [76]. HR: host rock; KB: red-clast karstic breccias; RHR: recrystallized host rock; Cc: calcite cement; Cs: calcite sediment; Dc: dolomite cement.

depleted than the surrounding host rock. $\delta^{18}\text{O}$ values range from -9 to -6.3‰VPDB, whereas $\delta^{13}\text{C}$ values are -0.5 to +0.8‰VPDB (Figure 9). Cc1 in the Yijianfang and Tumuxiuke Formations yielded $\delta^{18}\text{O}$ values between -7.8 and -3.6‰VPDB and $\delta^{13}\text{C}$ ranging from -0.3 to +2.1‰VPDB. Progressively depleted values of $\delta^{18}\text{O}$ are recorded by Cc2, which range between -9.1 and -4.8‰VPDB for $\delta^{18}\text{O}$ and between -0.5 and +3.8‰VPDB for $\delta^{13}\text{C}$. Cc3 has $\delta^{18}\text{O}$ values ranging from -11.7 to -7.1‰VPDB and $\delta^{13}\text{C}$ values ranging from -0.2 to +2.8‰VPDB. Cc3a that precipitated in vugs within the Lianglitage Formation shows $\delta^{18}\text{O}$ values between -11.3 and -8.6‰VPDB and $\delta^{13}\text{C}$ between +1.3 and +2.8‰VPDB, whereas Cc3b shows $\delta^{18}\text{O}$ ranging from -12.8 to -9.3‰VPDB and $\delta^{13}\text{C}$ from +1 to +2‰VPDB. Cc4 in the Yijianfang and Tumuxiuke Formations has $\delta^{18}\text{O}$ between -18.3 and -13.0‰VPDB and $\delta^{13}\text{C}$ from -1.1 to +1.7‰VPDB. Cc5 and Cc6, only present in the Yingshan and Yijianfang Formations, have heavier $\delta^{18}\text{O}$ values and more depleted $\delta^{13}\text{C}$ values than the previous diagenetic cements, with $\delta^{18}\text{O}$ values from -11.1 to -6.4‰VPDB and $\delta^{13}\text{C}$ values from -1.8 to -0.1‰VPDB for Cc5, and $\delta^{18}\text{O}$ values from -15.4 to -8.5‰VPDB and $\delta^{13}\text{C}$ values from -2.4 to -0.2‰VPDB for Cc6. Cc7b in the Yijianfang Formation has values of 18.3‰VPDB for $\delta^{18}\text{O}$ and -1.1‰VPDB for $\delta^{13}\text{C}$ (Figure 9).

The isotope equilibrium temperature equation of Craig [75] can be applied to calculate approximate temperatures of cement precipitation. We use the heaviest stable isotopic value of marine fluids obtained from host rocks and isotopic values reported for Middle Ordovician carbonates [76] (Figure 9). Precipitation of Cc0 within the host rocks is inferred to have occurred at ~25°C, whereas Cc1 precipitated at <20°C, Cc2 at ~30°C, Cc3 at <45°C, and Cc4 at <80°C. The presence of exotic minerals accompanying Cc5 in F5 fractures indicates that the system was open and that $\delta^{18}\text{O}_{\text{SMOW}}$ of the parental fluid probably had a different composition than the value assumed for Ordovician marine water so this method was rendered unreliable for these and subsequent cements.

4.2.2. Strontium Isotopes. The $^{87}\text{Sr}/^{86}\text{Sr}$ ratio of Yingshan Formation host rocks is 0.7088, whereas it ranges from 0.7087 to 0.7088 for the Yijianfang Formation, 0.7089 to 0.7090 for the Tumuxiuke Formation, and 0.7085 for the Lianglitage Formation. The matrix of karstic breccias within the Lianglitage Formation shows $^{87}\text{Sr}/^{86}\text{Sr}$ of 0.7099, well above that of the host rock (Figure 9).

Cs0 in mottle fabrics (Yijianfang Formation) shows values of 0.7091, and Cc1 (Tumuxiuke Formation) shows a ratio of 0.7087. Isotopic values for Cc3a (Yijianfang and Lianglitage Formations) vary between 0.7085 and 0.7088, and it is 0.7086 for Cc3b. Cc4 shows values from 0.7094 to 0.7102 in the Yijianfang Formation and 0.7093 to 0.7097 in the Tumuxiuke Formation. $^{87}\text{Sr}/^{86}\text{Sr}$ values for Cc5 and Cc6 (Yijianfang Formation) are 0.7090 for Cc5 and range between 0.7093 and 0.7094 for Cc6 (Figure 9). Due to their small size, we have no Sr data for Cc7 cements.

4.2.3. Fluid Inclusion Microthermometry. Most fracture and vug cements in all formations trapped primary aqueous fluid and hydrocarbon (oil) inclusions in fluid inclusion assem-

blages (FIA) occurring along various generations of growth zones or close-packed clusters within a single growth zone or in the core of host grains (Figure 10). Several FIAs of secondary aqueous and hydrocarbon FIs were also observed. The aqueous inclusions range from 5 to 25 μm in the long diameter, but most are <10 μm . The FIAs contain either single-phase liquid inclusions only or two-phase liquid-vapor inclusions. In a few cases, we observed inclusions containing also a solid phase which was typically opaque black or light amber, interpreted to potentially be a solid hydrocarbon phase (wax or bitumen). The solids appear only sporadically in a few inclusions within the same assemblage, so their phase ratios (liquid-vapor-solid) vary. Variations in phase ratios of inclusions within these FIAs are interpreted to indicate that the solid was trapped accidentally in the inclusions and not as a result of precipitation from the fluid. A summary of homogenization temperatures (T_h) and salinity of primary two-phase aqueous inclusions observed in various cements is presented in Figure 11 and Table 2.

Overall, the aqueous fluid inclusions show a wide range of T_h from ~50°C to 165°C for all cements, with temperature variation ranging from ~2°C to 40°C within individual FIAs. Ice melting temperatures also show a wide range from 1.1 to 11.1°C, corresponding to salinities of 0.4 to 19 wt% NaCl equivalents [77]. The eutectic (first ice melting) temperature of the inclusion fluids was observed at around -50°C, indicating that the aqueous fluid trapped in the inclusions can be adequately described as a $\text{H}_2\text{O}-\text{NaCl}-\text{CaCl}_2-(\pm\text{MgCl}_2)$ -type fluid. Melting of other phases at this temperature, such as antarcticite [77], was not observed due to the small size of the inclusions. However, one sample contained fluid inclusions in which we observed the melting of two solid phases during the freezing-heating runs. The first solid melted at temperatures ranging from -22.6°C to -21.2°C, interpreted to be hydrohalite, and the second melted at temperatures ranging from -12.6°C to -4.8°C, interpreted to be water ice. The melting of these two phases allowed us to determine that the aqueous fluid contained 0 to 3.9 wt% CaCl_2 and 7.7 to 15.7 wt% NaCl [77]. An analyzed F5 fracture shows a clear sequence of cement precipitation with zoned fluorite forming first, followed by barite and calcite (Cc5). All these cements trapped primary aqueous fluid inclusions that show a systematic temperature variation from ~80°C to 110°C in fluorite, from ~120 to 140° in barite, and ~60 to 100°C in late Cc5 calcite (Figure 11). The salinity of the fluids shows a similar trend that mirrors temperatures, ranging from 9.6 wt% to 10.5 wt% NaCl equivalents in fluorite, up to ~19 wt% NaCl equivalents in barite, and from 5.7 to 14.7 wt% NaCl equivalents in Cc5 (Figure 11).

Primary oil inclusions are present within Cc3, Cc4, and fluorite cements in all three formations but are absent in early Cc0 host rock, Cc1 fracture, and Cc2 vug cements. We have no primary oil inclusion data for Cc5 and Cc6 cements. FIAs of oil inclusions show both heterogeneous and apparent homogeneous liquid-to-vapor ratios within the same FIA at room temperature. Oil inclusions in FIAs with homogeneous liquid-to-vapor ratios show T_h ranging from 44 to 75°C (Table 2). The fluorescence color of the oil inclusions under UV light ranges from yellow to green in Cc3 calcite and F5

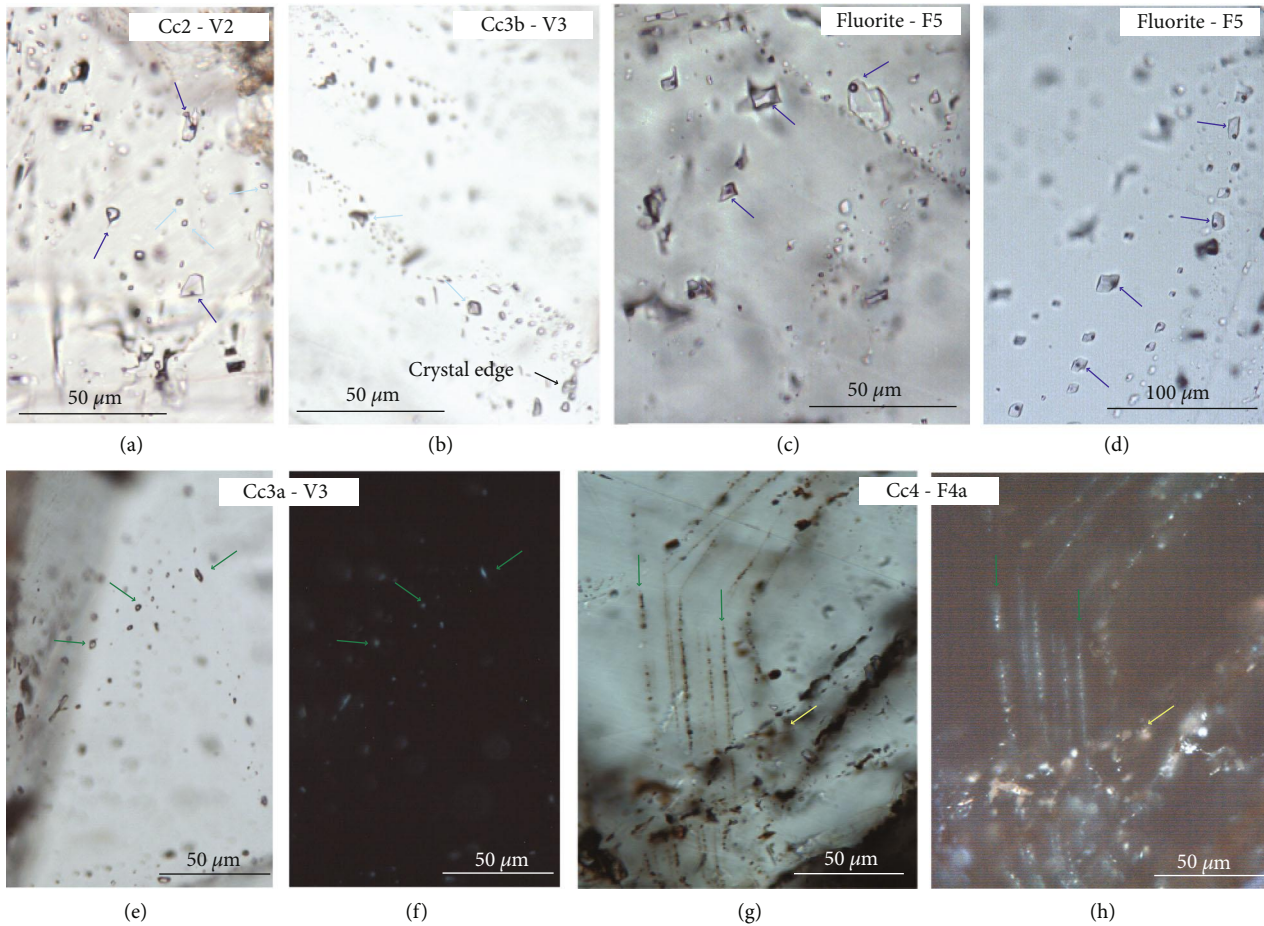


FIGURE 10: Photomicrographs of typical fluid inclusions. (a) Example of stretched inclusions: dark blue arrows highlight primary two-phase aqueous inclusions with inconsistent $L:V$ ratios and light blue arrows highlight primary single-phase aqueous inclusions. (b) Light blue arrows highlight pseudosecondary single-phase aqueous inclusions trapped along a plane that terminates at crystal edges. (c) Dark blue arrows highlight clustered primary two-phase aqueous inclusions with homogenous $L:V$ ratios. (d) Dark blue arrows highlight primary aqueous two-phase inclusions with homogenous $L:V$ ratios trapped along a growth zone. (e) Dark green arrows highlight primary three-phase oil ($L:V:S$) inclusions trapped along a growth zone. The solid phase is a hydrocarbon solid. (f) Blue fluorescence of oil inclusions in (e) under UV light. (g) Dark green arrows highlight primary single-phase oil inclusions trapped along growth zones. The light green arrow highlights a trail of secondary two-phase oil inclusions. (h) Blue (dark green arrows) and dull orange (light green arrow) fluorescence of oil inclusions in (g) under UV light.

fluorite cements of the Yijianfang Formation, and green to bright blue in Cc3 cements of the Lianglitage and Tumuxiuke Formations as well as subsequent Cc7 cement of the Yijianfang Formation (Figure 11).

5. Discussion

Discerning cavities formed by shallow (epigenetic) dissolution from those due to deep-seated (mesogenetic) dissolution is challenging since by definition, the cavities themselves cannot be sampled. In cases where cavities are small enough to be sampled by core (vugs), voids preserve scant evidence of their origin. In many cases, however, vugs and associated fractures within the studied carbonates contain cement linings and fills that can be used to obtain information about the physical and chemical conditions during the various stages of dissolution and cementation

that affected these rocks. Information about temperature, pressure, stress, and fluid compositions during deformation [40–44] is recorded in cements and fluid inclusions trapped within them. Cemented vugs and dissolution-enhanced fractures identified in this study are cut by subsequent generations of cemented vugs and fractures, indicating cements recorded conditions prior to and following dissolution. The sequence of structural diagenetic features identified in this study, and in particular the cements that precipitated within them, can be used to constrain the evolution of physical, chemical, and mechanical conditions that led to the formation of hydrocarbon-hosting cavities in the Halahatang area.

Although Middle-Lower and Upper Ordovician carbonate rocks show many similarities in their structural diagenetic evolution, not all features are present in all formations. Our sample suite allowed establishing the most complete

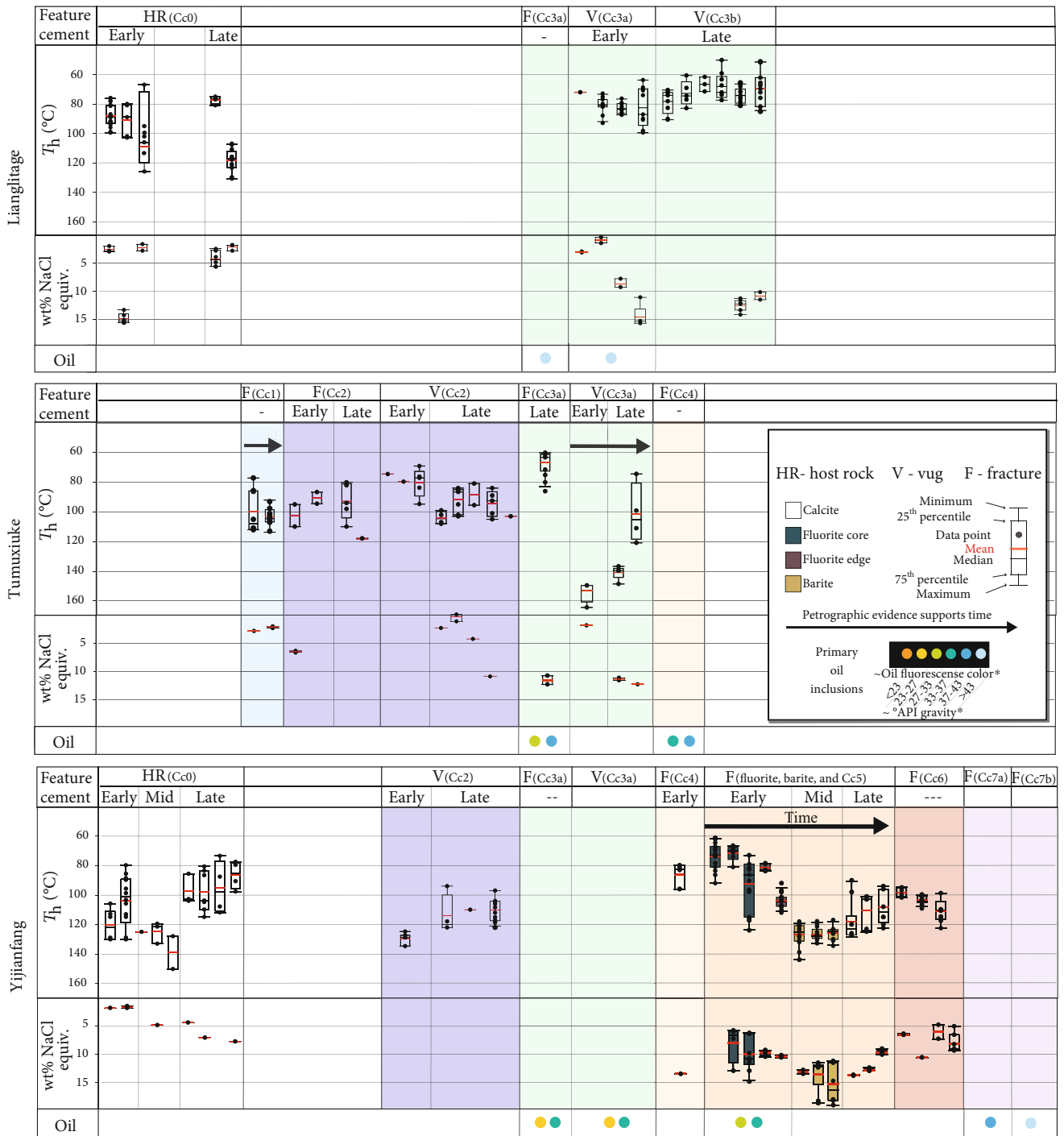


FIGURE 11: Box and whisker plots showing microthermometry results of two-phase aqueous inclusions (minimum trapping and salinity) for individual FIAs arranged by formation and diagenetic feature in chronological order.

paragenetic sequence for the Yijianfang Formation, which is presented below (Figure 12).

5.1. Diagenetic Environments

5.1.1. Stage 0: Marine Diagenesis. The $\delta^{18}O$ and $\delta^{13}C$ values of the host rocks are consistent with isotopic values inferred by Shields et al. [76] and Veizer et al. [78] for Middle Upper Ordovician marine carbonates (Figure 9). Therefore,

host rock cements (Cc0) most likely precipitated from marine pore fluids. However, $^{87}Sr/^{86}Sr$ ratios of the Tumuxiuke and Lianglitage Formations are slightly higher than the values expected for Upper Ordovician marine carbonates, probably due to the clay mineral content of the matrix in the mudstones and wackestones [79]. Low salinities, similar to those of seawater, of some fluid inclusions in Cc0 host rock cements support precipitation within the marine diagenetic realm (Figure 11). However, T_h —considered

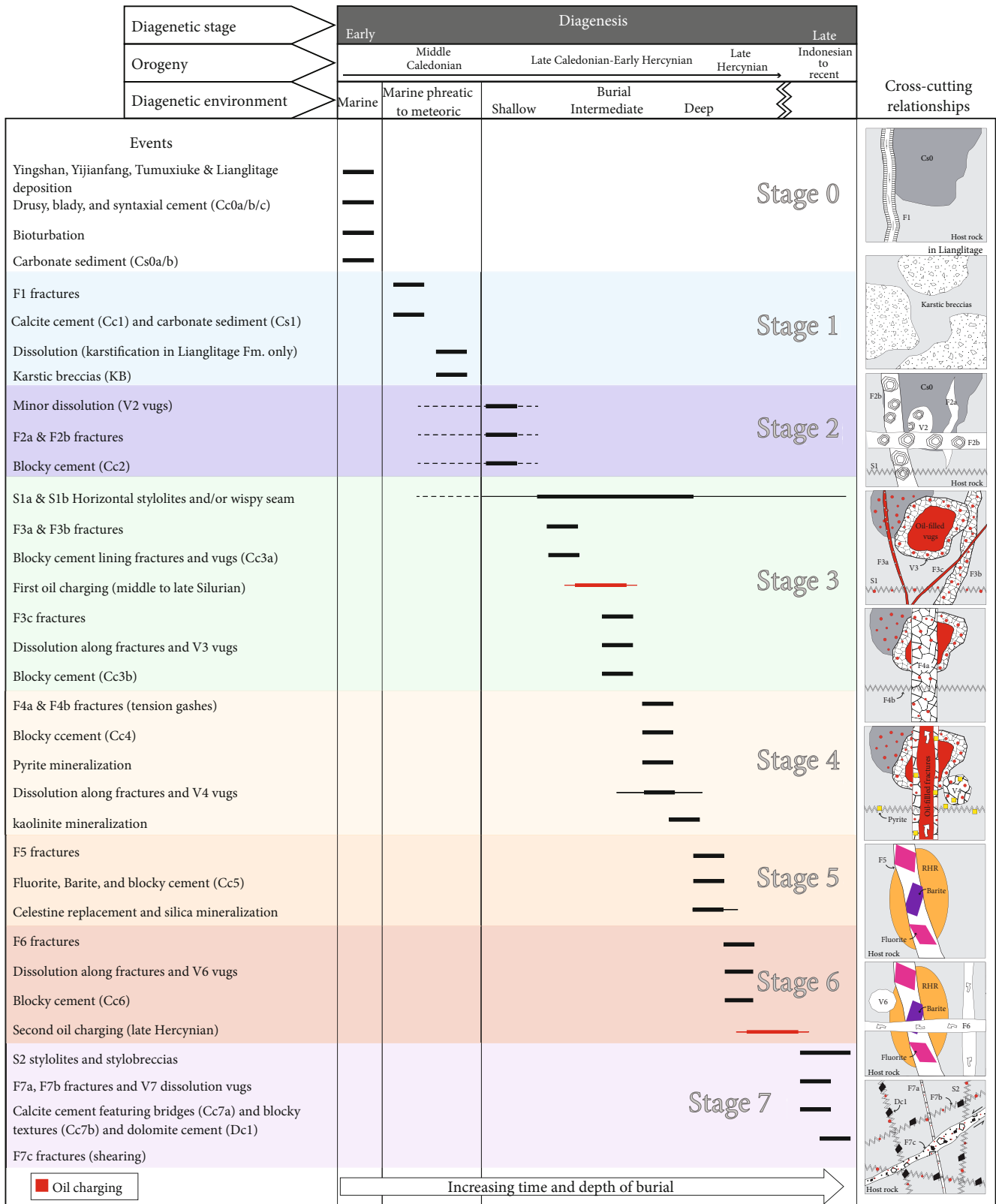


FIGURE 12: Summary of the diagenetic sequence in the studied Ordovician carbonates.

minimum trapping temperatures [80]—and salinities of some of the inclusions are highly variable and much higher than it would be expected for a shallow marine environment. Moreover, fluid inclusion temperatures are much higher than those calculated on the basis of oxygen isotopic contents. The high variability in T_h and salinities supports the inference that the high temperatures and salinities of such fluid inclusions are the result of reequilibration with burial fluids during progressive burial to higher depths [81, 82]. The reequilibration can be a combination of adjustment of the inclusions to new temperature and pressure conditions by stretching or changing the volume of the inclusions or by partial infiltration of new fluids, mixing with the inclusion fluids. The inferred reequilibration of inclusions suggests that caution must be taken if temperatures are correlated with burial thermal history models for timing constraints (e.g., [83]).

Our study shows that mottle fabrics are neither the result of penetrative surficial karstic processes nor deep diagenetic features but are burrows that were subsequently overprinted by mesogenetic dissolution. Channel-shaped mottle fabrics infilled with fragmented fossils support the interpretation that these are calcite-filled burrows characteristic of early diagenesis [84]. Cements in mottle fabrics and host rocks have similar geochemical characteristics indicating pores formed due to minor dissolution of the host rock. $^{87}\text{Sr}/^{86}\text{Sr}$ ratios higher than those of the host rocks may be due to the alteration of illite and kaolinite within intergranular pores of Cs0 [64, 85, 86] (Figure 9). Our results are broadly compatible with previous interpretations of mottled fabrics being the result of selective diagenetic alteration and subsequent infiltration of bitumen [35]. The irregularity of mottle fabric walls and their distribution may reflect dissolution caused by hydrocarbon-bearing fluids that upwelled from underlying hydrocarbon source rocks [22].

5.1.2. Stage 1: Marine Phreatic Diagenesis. Uplift processes, such as those experienced in the area during the Caledonian and Hercynian orogenies, typically lead to reduced temperatures and pressure and may be accompanied by substantial changes in pore-fluid composition due to deeper penetration of meteoric fluids from elevated recharge areas [87]. Such fluids can travel along fractures and cause dissolution, forming solution-enhanced fractures with irregular walls such as F1. Palisade calcite cements (Cc1) and internal sediment (Cs1) within F1 fractures are characteristic of precipitation within the phreatic-vadose level [8, 41, 88]. However, $\delta^{18}\text{O}$ and $\delta^{13}\text{C}$ isotopic values indicate precipitation from marine fluids [40]. Infiltrated meteoric waters could mix with pore waters so that fluids would show low, but nonzero, salinities. Low salinities of fluid inclusions in Cc1 cements within the overlying Tumuxiuke Formation support marine precipitation, but the high T_h suggest reequilibration during progressive burial [81]. Using a geothermal gradient of $28^\circ\text{C}/\text{km}$ for the Tabei Uplift during the Middle Ordovician [89], calculated temperatures of $<20^\circ\text{C}$ indicate that Cc1 cements precipitated very near the surface, consistent with precipitation in the Middle Ordovician [90–93] (Figure 13).

5.1.3. Stage 2: Marine to Shallow Burial Diagenesis. This stage was characterized by the onset of burial and formation of compaction-related fractures and stylolites (S1) as well as dissolution. Cc2 cements in F2 fractures and V2 vugs show $\delta^{13}\text{C}$ values similar to those of the host rock, whereas $\delta^{18}\text{O}$ values of these cements are slightly more depleted (Figure 9). This depletion suggests that Cc2 precipitated from marine fluids during progressive burial of the rock [94]. Estimated temperatures of 30°C indicate precipitation of Cc2 at ~ 220 m depth, within the shallow burial diagenetic environment [95]. Fluid inclusions within Cc2 in the Yijianfang and overlying formations show a range but generally higher temperatures, suggesting, again, reequilibration of the inclusions at higher burial depths. The $^{87}\text{Sr}/^{86}\text{Sr}$ ratio of these cements is similar to that of the host rocks (Figure 9), indicating high rock-fluid interaction [96]. A comparison with a representative burial history curve for the study area indicates that Middle Ordovician strata attained those depths around the end of the Ordovician (Figure 13). The lack of primary oil inclusions in Cc2 or earlier cements agrees with this timing, preceding the first stage of hydrocarbon generation in the Silurian [1, 61]. It is likely that similar fluids that caused stage 1 dissolution continued to cause corrosion of carbonates at this stage.

5.1.4. Stage 3: Intermediate Burial Diagenesis. This stage was characterized by the formation of F3 fractures and V3 vugs. The spatial association between F3, V3, and mottle fabrics indicates V3 most likely formed by the enlargement of dissolution-prone, more porous, diagenetically altered areas (mottle fabrics). Cc3 that precipitated in F3 fractures and V3 vugs shows depleted $\delta^{18}\text{O}$ values compared to the host rock indicating burial and precipitation from low- to medium-temperature formation waters (Figure 9). Calculated temperatures of $<45^\circ\text{C}$ indicate that Cc3 cements precipitated at ~ 625 m depth, within the intermediate burial diagenetic environment [17, 95], in contrast to the higher temperatures of fluid inclusions in overlying formations (Figure 11). The similarity of $\delta^{13}\text{C}$ values between Cc3 and the host rock indicates that carbon was buffered by the host rocks [94]. The $^{87}\text{Sr}/^{86}\text{Sr}$ ratio, similar to that of the host rock, also indicates the prevailing interaction between the fluid and the host limestone (Figure 9).

Cc3a filling V3 vugs and F3 fractures contains primary oil inclusions, indicating that oil was present in the system at the time of precipitation of these cements. Oil presence is further supported by bitumen in group 3 fractures and vugs. The first oil accumulation in the study area, derived from Cambrian source rocks [90], dates to the Late Caledonian–Early Hercynian period [1, 61]. This timing of oil generation and inferred depth for Cc3 cements is compatible with the formation and partial cementation of group 3 features in the Silurian (see Ukar et al. [93]). Heavy crude oil in the study area is rich in H_2S , and sulfur content may be as high as 2% [63]. A rise in the temperature of the reservoir caused by burial would trigger thermal decomposition of sulfur compounds to produce more H_2S [1]. Sulfur-rich oil can mix with water to create H_2SO_4 in a process similar to that which created Carlsbad Caverns in the Guadalupe Mountains (Texas, USA) [97]. Fluids, including hydrocarbons and acidic fluids associated

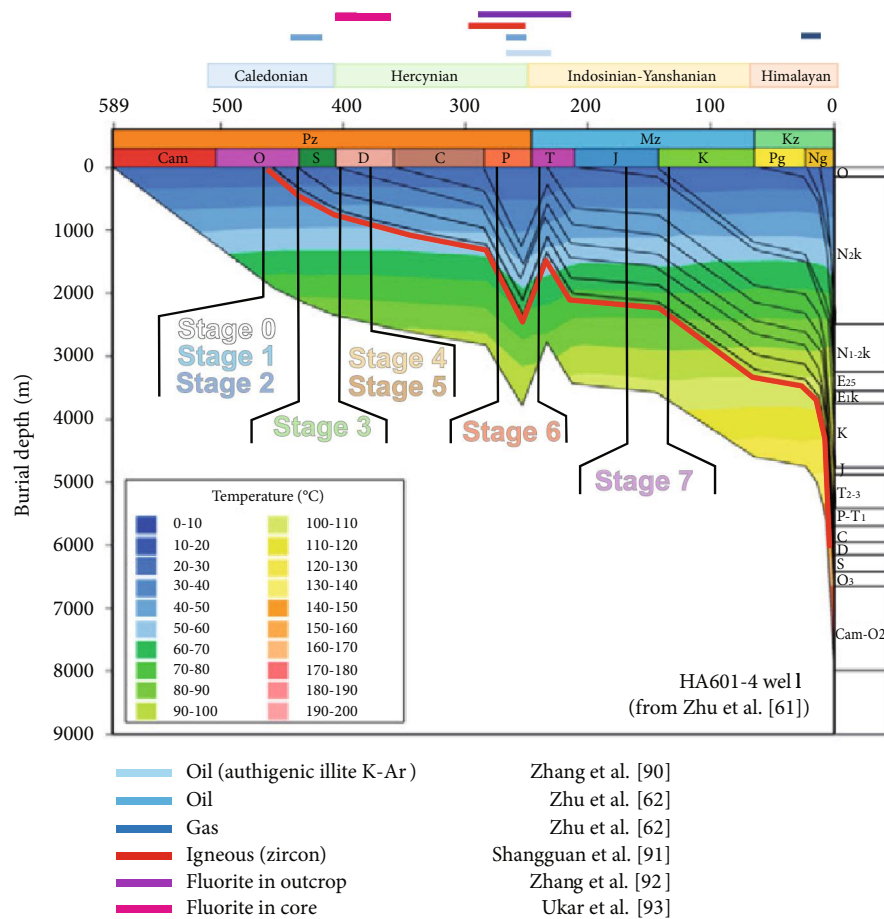


FIGURE 13: Estimated timing and depths of occurrence of the diagenetic stages described in the text in the context of a burial history model calculated for one of the wells in our study area (burial history curve from Zhu et al. [61]; well HA601-4).

with sulfur-rich oil, flowed along F3 fractures and S1a stylolites causing localized dissolution and formation of vugs. Host rock reworking and dissolution associated with burrowing that led to the formation of early diagenetic mottle fabrics generated up to 1-3% of porosity within these areas, allowing for infiltration of dissolving fluids and localization of subsequent dissolution around dissolution-prone mottle fabrics. Where an F3 and/or S1a encountered a dark mottle, porosity (secondary) increased giving the rock the aspect of pseudobreccia [35].

5.1.1.5. Stages 4 to 7: Deep Burial Diagenesis. Cc4 that precipitated within F4 fractures and V4 vugs shows yet more depletion in $\delta^{18}\text{O}$ compared to the host rock. The lower values in $\delta^{18}\text{O}$ indicate further burial of the rocks and circulation of high-temperature formation waters (Figure 9). Cc2 to Cc4 follow a general trend of slight increase in $\delta^{13}\text{C}$ and decrease in $\delta^{18}\text{O}$ that suggests rock-water interaction at progressively more elevated temperatures. Calculated temperatures of $<80^\circ\text{C}$ indicate that Cc4 precipitated at ~ 2000 m depth, within the deep burial diagenetic environment [17, 95]. The similarity of $\delta^{13}\text{C}$ values between Cc4 and host rocks indicates that carbon was buffered by the host carbonate [94]. However, high $^{87}\text{Sr}/^{86}\text{Sr}$ values of these calcites suggest incorporation of

radiogenic Sr derived from older rocks such as evaporitic Cambrian strata [98, 99], from the Precambrian basement [100, 101], and/or alteration of feldspars, clays, and other clastic terrigenous minerals present within deeper strata [102].

Cc5 and Cc6 show more depleted $\delta^{13}\text{C}$ and/or heavier $\delta^{18}\text{O}$, departing from the general trend of increasing temperatures (Figure 9) and pointing to fluid mixing in a hydrologically open system [16, 40]. Precipitation of noncarbonate minerals along F5 (fluorite, barite, and celestite) supports changes in fluid chemistry and/or temperature. Infiltration of high-temperature fluids is supported by generally high FI temperatures within F5 and F6 cements (Figure 11). The partial dissolution experienced by some F4 fractures could have been caused by such high-temperature fluids, possibly from a deeper source. This is supported by the parallel and systematic change of temperatures and salinity, showing increasing then decreasing trends, from earlier fluorites to late calcite cements in F5 fractures. The oxidation of pyrite associated with F4 and stylolites would be accompanied by a pH decrease creating an acidic environment that would drive dissolution [103, 104]. Corrosive fluids may have also been associated with subsequent precipitation of fluorite [16].

A 400 ± 37 Ma isochron age of an F5 fracture reported by Ukar et al. [93] indicates formation and subsequent mineral

filling by the end of the Devonian, consistent with inferred depths of calcite precipitation, reached by Ordovician strata at that time (Figure 13). $^{87}\text{Sr}/^{86}\text{Sr}$ values of subsequent Cc6 that precipitated in fractures are consistent with isotopic values of Middle Permian magmas (~295–263 Ma) [91, 92, 105] suggesting that Cc6 acquired its high Sr isotope ratios by incorporating radiogenic Sr derived from magmatic fluids [64, 79, 84, 86, 106].

Dolomite (Dc1) and calcite cement (Cc7) mineralization associated with F7 fractures, V7 vugs, and stylobreccias (S2, fault breccias) indicates the presence of Mg-rich fluids in the system following Permian activity. The penetrative deformation recorded by these structures most likely occurred in the Jurassic–Early Cretaceous ([93]).

Younger Cc7 cements in the Yijianfang Formation contain primary oil inclusions with higher API gravity values (dull to light blue color; ~40–45 API° gravity) than older Cc3 and fluorite cements (yellow to green color; ~30–35 API° gravity), which is consistent with increased oil maturity in the system over time (Figure 11). The UV light fluorescence color of oil inclusions in Cc3 and Cc4 cements in the overlying Tumuxiuke and Lianglitage Formations is more mature (green to light blue) than that in equivalent features within the Yijianfang Formation and is similar to that in Cc7 within the Yijianfang Formation. This trend is the opposite of that expected for variations in thermal maturity of oils with depth [107]. Without a constraint on the composition of the oils, possible explanations for the variations in the UV light fluorescence color of the oils between formations include locally occurring factors such as biodegradation, water washing, and migration fractionation ([107]) within a potentially weakly interconnected fluid system across the clay-rich Tumuxiuke Formation at the time of Cc3 cementation.

5.2. Dissolution and Fluid Pathways. In the Tabei Uplift, a seismic interpretation of the top Ordovician illustrates an erosional topography and seismic geomorphologic patterns related to the unconformity, with numerous sinuous fluvial channels and canyons, fluvial valleys, sinkholes, and tower karsts and hills [2, 108, 109]. Intensive karstification was hypothesized to be related to a prolonged sea level fall and subaerial exposure, which coincided with a major glaciation at the end of the Ordovician [110].

However, in the Halahatang area, the only breccias we encountered that resemble karstic fillings are the ones present in the Lianglitage Formation. Localization of silt quartz, clays, and iron oxides to within brecciated areas indicate that such sediments were most likely transported into cavities during subaerial exposure (epigenetic dissolution). Similar sediment-filled cavities have been extensively documented in cores of the Lianglitage Formation in other study areas [27, 111]. Moreover, the presence of widespread near-surface paleokarst is evident in seismic patterns, where topographic relief of 100s of meters resembling the modern topography of the Guilin active karst region is visible at the top of Upper Ordovician carbonates. The fracture-cavity network has been related to incised valleys,

the result of an ancestral river at the top of the Lianglitage Formation [112].

Karstic breccias are absent in the Yijianfang Formation in our study area. Early diagenetic features here are mottle fabrics, but these show similar isotopic and lithologic compositions as the host rock indicating that they formed in situ due to minor reworking and dissolution associated with burrowing. Primary porosity associated with near-surface mottle fabric dissolution was <3%, similar to the 1–3% of the matrix. The 5–12% porosity reported for the reservoir [113] must have therefore been caused by subsequent dissolution. Textural and isotopic evidence shows that the majority of the dissolution recorded by Yijianfang Formation strata occurred within the intermediate and deep diagenetic environments (mesogenetic dissolution). Although the Lianglitage and Tumuxiuke Formations contain evidence for mesogenetic dissolution, some of the structural diagenetic features identified in the Yijianfang Formation are absent in the overlying formations (Table 1). This difference in structural diagenesis between the Lianglitage and Yijianfang Formations suggests a hydrologic isolation by the presence of caprock of the compact muddy limestone stratum of the Tumuxiuke Formation in between [25, 57].

However, petrographic, SEM-CL, and isotopic compositions of vug- and fracture-filling cements of many of the identified structural diagenetic features are the same across the Tumuxiuke Formation indicating that the carbonate rocks below and above this capping horizon were somehow connected, in agreement with observations by Zhu et al. [114]. The close association between fractures and dissolution vugs indicates corrosive fluids flowed along fractures, some of which must have extended vertically across formations for tens to hundreds of meters. Diagenetic cements that precipitated along stylolites indicate that these also acted as pathways rather than barriers to flow.

5.3. Multiple Shallow and Deep Dissolution Events. Multiple karst events related to surficial exposure and shallow to deeply penetrating groundwater are widespread in Paleozoic carbonate rock sequences, and groundwater can penetrate to great depths and cause dissolution (e.g., [115]). Dissolution along faults is also widely accepted [18, 20, 116, 117]. But the evidence we found of repeated dissolution and precipitation primarily at great depth and not necessarily associated with exposure surfaces or groundwater contemporaneous with exposure raises a question of how useful the term “paleokarst” is to describe both (1) features with clear linkages to surficial or near-surface processes and (2) dissolution at great depth owing to corrosive fluids penetrating along faults and fractures that may have uncertain or no connection with karst topography or groundwater. We contend that the structures we describe are probably not usefully categorized as paleokarst, since processes operating at depth may markedly differ in characteristics and timing of dissolution and may have patterns that differ substantially from those governed by paleotopography and other near-surface controls. For example, corrosive fluids might catalyze fault slip and fault porosity evolution as a consequence of chemical-mechanical interaction (e.g., [118]). We prefer to identify

and categorize dissolution features with a descriptive terminology.

Dissolution at deep burial depths on a massive scale (up to 20%) has been doubted [119, 120]. Ehrenberg et al. [119] and Ehrenberg [120] argued that burial dissolution in carbonates would not contribute significantly to a net increase in carbonate reservoir porosity. Furthermore, they stated that pore waters highly undersaturated with respect to calcite would in most cases be neutralized very rapidly during migration before reaching carbonate reservoirs and that consequently dissolution would be limited to a narrow reaction front along fractures in case acidic waters would reach the reservoir level. But in the case of Halahatang, the prevalence of active faults resulted in multistage reactivation of faults both in shear and in extension, and the formation of porous fault rock and dissolution-enhanced cavities, as evidenced by stylolites and associated fractures and vugs as well as fault rocks exposed in nearby outcrops ([93]) and cavities imaged near faults [23, 36, 37, 121]. On the basis of fault porosity and abundance and core observations, Ukar et al. [93] suggest that local mesogenetic porosity enhancement of as much as 5–10% is plausible. Both porous fault rock and dissolution-enhanced cavities and fractures could provide hydrocarbon storage and migration pathways and be responsible for decimeter-scale bit drops and large volumes of drilling mud losses.

6. Conclusions

Petrographic, geochemical, and microthermometric results from ~230 samples from 16 wells across the Halahatang oilfield indicate that Middle Ordovician rocks underwent multiple stages of fracturing, dissolution, and mineralization.

Unlike the overlying Lianglitage Formation where near-surface karstic breccias are widespread, in the Yijianfang Formation we found no evidence for cave-fill sediments that would have resulted from penetrative epigenetic karstic processes. Near-surface diagenetic features in the Yijianfang Formation are restricted to mottle fabrics filled with allochthonous carbonate silt and cements formed as a result of bioturbation (stage 0). Primary porosity associated with near-surface dissolution is similar to that of unaltered host rocks (1–3%), arguing against a significant increase in porosity-permeability related to this event. Subsequent secondary dissolution caused porosity within mottle fabrics to increase by as much as 10%.

Crosscutting relationships between sequences of partially cemented fractures and vugs that postdate mottle fabrics and stable isotopic compositions of calcite cement fillings indicate that multiple subsequent structural diagenetic stages occurred within the shallow to deep burial diagenetic environments. $\delta^{18}\text{O}$ analyses tied to geothermal gradients indicate cement precipitation within the shallow (~220 m, stages 1–2), intermediate (~625 m, stage 3), and deep (~2000 m, stages 4–7) diagenetic environments. The presence of oil fluid inclusions in cements at stage 3 and younger confirms the presence of hydrocarbons in the system at the time of void-filling mineral precipitation.

Stages 0–2 dissolution was associated with possible infiltration of meteoric fluids, whereas stages 3–4 were likely caused

by acidic fluids associated with Middle-Late Silurian and Devonian-Permian hydrocarbon generation. Stage 5 was associated with fluorite and barite mineralization with a possible deeper fluid source. An isochron age of 400 ± 37 Ma confirms stage 5 dissolution and subsequent cementation occurred by the end of the Devonian. Stage 6 calcite has elevated $^{87}\text{Sr}/^{86}\text{Sr}$ as a result of external fluid infiltration associated with Permian igneous activity. Stage 7 stylolites and fractures were associated with Mg-rich fluids and Jurassic-Cretaceous deformation. Fluctuating, but high (80–120°C), homogenization temperatures and generally high salinities (5–20% NaCl equiv.) of fluid inclusions trapped within late calcite cements indicate potential reequilibration of the fluid inclusions with deeper, higher-temperature fluids. Close association of fractures with vugs of all stages and mineralization along stylolites indicate that they both acted as corrosive-fluid pathways.

Data Availability

The data that support the findings of this study are provided in the supplementary material.

Conflicts of Interest

No conflict of interest was declared.

Acknowledgments

We are grateful to Haijun Yang, Zhibin Huang, Chunyan Qi, Emily Xing, Wenqing Pan, Kuanzhi Zhao, Yu Ye, and others from CNPC for the access to the cores and fruitful discussions. This manuscript benefited from discussions with Bob Loucks, Qilong Fu, Chaozhong Ning, and Livia Sivila. We would like to thank Sara Elliott for her help with SEM analyses and image processing and Beverly Dejarnett for her help in understanding bioturbation and burrowing processes in carbonate rocks. The publication of this manuscript is authorized by the Director of the Bureau of Economic Geology. This study was funded by CNPC-USA and CNPC-Tarim Oilfield Company and by the Fracture Research and Application Consortium. Our work on fracture pattern development and diagenesis is partly supported by grant DE-FG02-03ER15430 from the Chemical Sciences, Geosciences and Biosciences Division, Office of Basic Energy Sciences, Office of Science, U.S. Department of Energy.

Supplementary Materials

The supplementary material includes stable isotopic analyses, radiogenic isotopic analyses, and fluid inclusion analyses. Supplementary Material I: stable isotopic analyses. Supplementary Material II: radiogenic isotopic analyses. Supplementary Material III: fluid inclusion analyses. (*Supplementary Materials*)

References

- [1] G. Zhu, X. Liu, H. Yang et al., "Genesis and distribution of hydrogen sulfide in deep heavy oil of the Halahatang area

- in the Tarim Basin, China,” *Journal of Natural Gas Geoscience*, vol. 2, no. 1, pp. 57–71, 2017.
- [2] H. Zeng, R. Loucks, X. Janson et al., “Three-dimensional seismic geomorphology and analysis of the Ordovician paleokarst drainage system in the central Tabei Uplift, northern Tarim Basin, western China,” *American Association of Petroleum Geologists Bulletin*, vol. 95, no. 12, pp. 2061–2083, 2011.
- [3] H. Zeng, G. Wang, X. Janson et al., “Characterizing seismic bright spots in deeply buried, Ordovician Paleokarst strata, central Tabei Uplift, Tarim Basin, Western China,” *Geophysics*, vol. 76, no. 4, pp. B127–B137, 2011.
- [4] L. H. Liu, Y. S. Ma, B. Liu, and C. L. Wang, “Hydrothermal dissolution of Ordovician carbonates rocks and its dissolution mechanism in Tarim Basin, China,” *Carbonates and Evaporites*, vol. 32, no. 4, pp. 525–537, 2017.
- [5] J. Liu, Z. Li, L. Cheng, and J. Li, “Multiphase calcite cementation and fluids evolution of a deeply buried carbonate reservoir in the Upper Ordovician Lianglitag Formation, Tahe Oilfield, Tarim Basin, NW China,” *Geofluids*, vol. 2017, Article ID 4813235, 19 pages, 2017.
- [6] R. G. C. Bathurst, *Carbonate sediments and their diagenesis*, Elsevier, New York, 1975.
- [7] K. C. Lohmann, “Geochemical patterns of meteoric diagenetic systems and their application to studies of paleokarst,” in *Paleokarst*, N. P. James and P. W. Choquette, Eds., pp. 58–80, Springer-Verlag, New York, 1988.
- [8] N. P. James and P. W. Choquette, *Paleokarst*, Springer-Verlag, New York, 1988.
- [9] V. P. Wright, “Paleokarst: types, recognition, controls and associations,” in *Paleokarsts and Paleokarstic Reservoirs*, V. P. Wright, M. Esteban, and P. L. Smart, Eds., vol. 2 of Occasional Publication Series, pp. 56–88, University of Reading, P.R.I.S, 1991.
- [10] M. Tucker, “Carbonate diagenesis and sequence stratigraphy,” *Sedimentology Review*, P. Wright, Ed., vol. 1, pp. 51–72, 1993.
- [11] K. J. Cunningham and C. Walker, “Seismic-sag structures in tertiary carbonate rocks beneath southeastern Florida, USA—evidence for hypogene speleogenesis?,” *Hypogene Speleogenesis and Karst Hydrogeology of Artesian Basins, Special paper*, A. B. Klimchouk and D. C. Ford, Eds., vol. 1, pp. 151–158, 2009.
- [12] P. W. Choquette and L. C. Pray, “Geologic nomenclature and classification of porosity in sedimentary carbonates,” *AAPG Bulletin*, vol. 54, pp. 207–250, 1970.
- [13] M. R. Giles and J. D. Marshall, “Constraints on the development of secondary porosity in the subsurface: re-evaluation of processes,” *Marine and Petroleum Geology*, vol. 3, no. 243, p. 255, 1986.
- [14] S. J. Mazzullo and P. M. Harris, “An overview of dissolution porosity development in the deep-burial environment, with examples from carbonate reservoirs in the Permian Basin,” in *Permian Basin Plays-Tomorrow’s Technology Today*, M. Candelaria, Ed., pp. 89–91, West Texas Geological Society (and Permian Basin Section of Society for Sedimentary Geology), 1991.
- [15] P. Wright and P. M. Harris, *Carbonate dissolution and porosity development in the burial (mesogenetic) environment*, 2013, Search and Discovery Article, #50860.
- [16] M. Esteban and C. Taberner, “Secondary porosity development during late burial in carbonate reservoirs as a result of mixing and/or cooling of brines,” *Journal of Geochemical Exploration*, vol. 78–79, pp. 355–359, 2003.
- [17] H. G. Machel, “Investigations of burial diagenesis in carbonate hydrocarbon reservoir rocks,” *Journal of the Geological Association of Canada*, vol. 32, p. 3, 2005.
- [18] B. Ronchi, *Hydrogeologische karakterisatie en modellering van de onverzadigde zone in het tufkrijt van de Maastricht Formatie te Vechmaal (Zuid-Limburg)*, [M.S. thesis], KU Leuven, Earth and Environmental Sciences, 2009.
- [19] J. Garland, J. Neilson, S. E. Laubach, and K. J. Whidden, “Advances in carbonate exploration and reservoir analysis,” *Geological Society, London, Special Publications*, vol. 370, no. 1, pp. 1–15, 2012.
- [20] W. Narr and E. Flodin, *Fractures in steep-rimmed carbonate platforms: comparison of Tengiz Reservoir, Kazakhstan, and outcrops in Canning Basin, NW Australia*, p. 31, 2012, American Association of Petroleum Geologists, Search and Discovery Article, #20161.
- [21] Q. Yixiong, C. Taberner, Z. Senlin, Y. Donghua, and W. Rongying, “Diagenesis comparison between epigenetic karstification and burial dissolution in carbonate reservoirs—an instance of Ordovician carbonate reservoirs in Tahe and Tazhong regions, Tarim Basin,” *Marine Petroleum Geology*, vol. 12, no. 2, pp. 1–7, 2007.
- [22] Z. Jin, D. Zhu, W. Hu, X. Zhang, J. Zhang, and Y. Song, “Mesogenetic dissolution of the middle Ordovician limestone in the Tahe oilfield of Tarim Basin, NW China,” *Marine and Petroleum Geology*, vol. 26, no. 6, pp. 753–763, 2009.
- [23] K. Ma and J. Hou, *Fault controlling of non-exposed karst reservoir in Halahatang District in North Tarim Basin*, 2015, Search and Discovery Article, 10800.
- [24] J. Y. Gu, “Characteristics and evolutionary model of karst reservoir of Lower Ordovician carbonate rocks in Lunnan area of Tarim Basin (in Chinese with English abstract),” *Journal of Palaeogeography*, vol. 1, pp. 54–60, 1999.
- [25] W. Zhao, A. Shen, Z. Qiao, J. Zheng, and X. Wang, “Carbonate karst reservoirs of the Tarim Basin, Northwest China: types, features, origins, and implications for hydrocarbon exploration,” *Interpretation*, vol. 2, no. 3, pp. SF65–SF90, 2014.
- [26] K. Zhao, Y. Dang, D. Zheng, B. Liang, Q. Zhang, and J. Li, “Characteristics of karst reservoir in the Ordovician buried hills of the Halahatang areas, northern Tarim Basin,” *Carso-logica Sinica*, vol. 34, pp. 171–178, 2015.
- [27] H. Fu, J. Han, W. Meng et al., “Forming mechanism of the Ordovician karst carbonate reservoirs on the northern slope of central Tarim Basin,” *Natural Gas Industry B*, vol. 4, no. 4, pp. 294–304, 2017.
- [28] G. Wu, E. Xie, Y. Zhang, H. Qing, X. Luo, and C. Sun, “Structural diagenesis in carbonate rocks as identified in fault damage zones in the northern Tarim Basin, NW China,” *Minerals*, vol. 9, no. 6, p. 360, 2019.
- [29] G. Q. Xu, S. G. Liu, G. R. Li, H. Z. Wu, and X. B. Yan, “Comparison of tectonic evolutions and petroleum geological conditions in Tazhong and Tabei palaeohighs in Tarim Basin,” *Oil and Gas Geology*, vol. 26, pp. 114–129, 2005.
- [30] Z. D. Bao, Y. C. Qi, Z. J. Jin et al., “Karst development response to sea-level fluctuation: a case from the Tarim area in the Early Paleozoic,” *Acta Geologica Sinica*, vol. 81, pp. 205–211, 2007.
- [31] M. Hu, X. Fu, Q. Cai, W. Yang, and W. Zhu, “Characteristics and genetic model of karst reservoirs of Ordovician

- Yingshan-Yijianfang Formation in Halahatang area, northern Tarim Basin," *Geology in China*, vol. 41, pp. 1476–1486, 2014.
- [32] Y. Dan, B. Liang, J. Cao, Q. Zhang, Y. Hao, and J. Li, "Characteristics and solution intensity of karst formations in Ordovician carbonates in the Halahatang area of the northern Tarim Basin," *Petroleum Geology & Experiment*, vol. 37, pp. 582–590, 2015.
- [33] T. Liao, J. Hou, L. Chen, W. Yang, and Y. Dong, "Evolutionary model of the Ordovician karst reservoir in Halahatang oilfield, northern Tarim Basin," *Acta Petrolei Sinica*, vol. 36, pp. 1380–1391, 2015.
- [34] T. Liao, J. Hou, L. Chen, W. Yang, Y. Dong, and X. Bai, "Fault controlling on non-exposed karst fracture-vug reservoirs of the Ordovician in Halahatang oilfield, northern Tarim Basin," *Journal of Palaeogeography*, vol. 18, pp. 221–235, 2016.
- [35] Q. Fu, "Characterization and discrimination of paleokarst breccias and pseudobreccias in carbonate rocks: Insight from Ordovician strata in the northern Tarim Basin, China," *Sedimentary Geology*, vol. 382, pp. 61–74, 2019.
- [36] G. Wu, L. Gao, Y. Zhang, C. Ning, and E. Xie, "Fracture attributes in reservoir-scale carbonate fault damage zones and implications for damage zone width and growth in the deep subsurface," *Journal of Structural Geology*, vol. 118, pp. 181–193, 2019.
- [37] G. Wu, Y.-S. Kim, Z. Su, P. Yang, D. Ma, and D. Zheng, "Segment interaction and linkage evolution in a conjugate strike-slip fault system from the Tarim Basin, NW China," *Marine and Petroleum Geology*, vol. 112, article 104054, 2020.
- [38] A. N. Palmer, "Origin and morphology of limestone caves," *Geological Society of America Bulletin*, vol. 103, no. 1, pp. 1–21, 1991.
- [39] C. L. Cazarin, R. A. Ennes-Silva, F. H. Bezerra, L. F. Borghi, A. S. Auler, and A. B. Klimchouk, *Hypogenic karst dissolution in carbonate rocks has implications for karstified carbonate reservoirs*, 2016, Search and Discovery Article, #41792.
- [40] C. Moore and W. J. Wade, *Carbonate Reservoirs: Porosity and diagenesis in a sequence stratigraphic framework*, 2013.
- [41] A. Travé, F. Calvet, A. Soler, and P. Labaume, "Fracturing and fluid migration during Palaeogene compression and Neogene extension in the Catalan Coastal Ranges, Spain," *Sedimentology*, vol. 45, no. 6, pp. 1063–1082, 1998.
- [42] A. Travé, P. Labaume, and J. Vergés, "Fluid systems in foreland fold-and-thrust belts: an overview from the southern Pyrenees," in *Thrust Belts and Foreland Basins: From Fold Kinematics to Hydrocarbon Systems*, O. Lacombe, J. Lavé, F. Roure, and J. Vergés, Eds., Springer Publications, Berlin, 2005.
- [43] N. Vilasi, J. Malandain, L. Barrier et al., "From outcrop and petrographic studies to basin-scale fluid flow modelling: The use of the Albanian natural laboratory for carbonate reservoir characterisation," *Tectonophysics*, vol. 474, no. 1–2, pp. 367–392, 2009.
- [44] L. André, M. Azaroual, and A. Menjoz, "Numerical simulations of the thermal impact of supercritical CO₂ injection on chemical reactivity in a carbonate saline reservoir," *Transport in Porous Media*, vol. 82, no. 1, pp. 247–274, 2010.
- [45] L. Tang, T. Huang, H. Qiu et al., "Fault systems and their mechanisms of the formation and distribution of the Tarim Basin, NW China," *Journal of Earth Science*, vol. 25, no. 1, pp. 169–182, 2014.
- [46] L. Tunini, I. Jiménez-Munt, M. Fernandez, J. Vergés, and A. Villaseñor, "Lithospheric mantle heterogeneities beneath the Zagros Mountains and the Iranian Plateau: a petrological-geophysical study," *Geophysical Journal International*, vol. 200, no. 1, pp. 596–614, 2015.
- [47] Y. G. Xu, X. Wei, Z. Y. Luo, H. Q. Liu, and J. Cao, "The Early Permian Tarim Large Igneous Province: main characteristics and a plume incubation model," *Lithos*, vol. 204, pp. 20–35, 2014.
- [48] Q. M. Wang, T. Nishidai, and M. P. Coward, "The Tarim Basin, NW China: formation and aspects of petroleum geology," *Journal of Petroleum Geology*, vol. 15, no. 1, pp. 5–34, 1992.
- [49] C. Z. Jia, *Tectonic Characteristics and Petroleum, Tarim Basin, China*, Petroleum Industry Press, 1997.
- [50] J. W. Cui, Z. M. Tang, J. F. Deng, Y. J. Yue, L. S. Meng, and Q. F. Yu, *Faults of the Altya Area*, Geological Press, Beijing, 1999.
- [51] J. Gao, "Paleozoic tectonic evolution of the Tianshan orogen, northwestern China," *Tectonophysics*, vol. 287, no. 1–4, pp. 213–231, 1998.
- [52] T.-G. Wang, F. He, C. Wang, W. Zhang, and J. Wang, "Oil filling history of the Ordovician oil reservoir in the major part of the Tahe oilfield, Tarim Basin, NW China," *Organic Geochemistry*, vol. 39, no. 11, pp. 1637–1646, 2008.
- [53] C. S. Lin, H. J. Yang, J. Y. Liu et al., "Paleostructural geomorphology of the Paleozoic central uplift belt and its constraint on the development of depositional facies in the Tarim Basin," *Science China Earth Sciences*, vol. 52, no. 6, pp. 823–834, 2009.
- [54] J. Yu, Z. Li, and L. Yang, "Fault system impact on paleokarst distribution in the Ordovician Yingshan Formation in the central Tarim Basin, Northwest China," *Marine and Petroleum Geology*, vol. 71, pp. 105–118, 2016.
- [55] C. Z. Jia, "Structural characteristics and oil/gas accumulative regularity in Tarim Basin," *Xinjiang Petroleum Geology*, vol. 20, no. 3, pp. 177–183, 1999.
- [56] L. J. Tang, L. X. Qi, H. J. Qiu et al., "Poly-phase differential fault movement and hydrocarbon accumulation of the Tarim Basin, NW China," *Acta Petrologica Sinica*, vol. 28, no. 8, pp. 2569–2583, 2012.
- [57] C. Xiangchun, T.-G. Wang, L. Qiming, and O. Guangxi, "Charging of Ordovician reservoirs in the Halahatang Depression (Tarim Basin, NW China) determined by oil geochemistry," *Journal of Petroleum Geology*, vol. 36, no. 4, pp. 383–398, 2013.
- [58] Y.-J. Li, Y. Zhao, L.-D. Sun et al., "Meso-Cenozoic extensional structures in the northern Tarim Basin, NW China," *International Journal of Earth Sciences*, vol. 102, no. 4, pp. 1029–1043, 2013.
- [59] C. Lin, H. Yang, J. Liu et al., "Sequence architecture and depositional evolution of the Ordovician carbonate platform margins in the Tarim Basin and its response to tectonism and sea-level change," *Basin Research*, vol. 24, no. 5, pp. 559–582, 2012.
- [60] D. H. Li, D. G. Liang, C. Z. Jia, G. Wang, Q. Z. Wu, and D. F. He, "Hydrocarbon accumulation in Tarim Basin, China," *AAPG Bulletin*, vol. 80, no. 10, pp. 1587–1603, 1996.
- [61] G. Zhu, S. Zhang, J. Su et al., "The occurrence of ultra-deep heavy oils in the Tabei Uplift of the Tarim Basin, NW China," *Organic Geochemistry*, vol. 52, pp. 88–102, 2012.
- [62] G. Zhu, J. Su, H. Yang et al., "Formation mechanisms of secondary hydrocarbon pools in the Triassic reservoirs in the northern Tarim Basin," *Marine and Petroleum Geology*, vol. 46, pp. 51–66, 2013.

- [63] X. Chang, B. Shi, Z. Han, and T. Li, “C₅-C₁₃ light hydrocarbons of crude oils from northern Halahatang oilfield (Tarim Basin, NW China) characterized by comprehensive two-dimensional gas chromatography,” *Journal of Petroleum Science and Engineering*, vol. 157, pp. 223–231, 2017.
- [64] J. A. D. Dickson, I. P. Montanez, and A. H. Saller, “Hypersaline burial diagenesis delineated by component isotopic analysis, Late Paleozoic Limestones, West Texas,” *Journal of Sedimentary Research*, vol. 71, no. 3, pp. 372–379, 2001.
- [65] R. G. Loucks, R. M. Reed, S. C. Ruppel, and D. M. Jarvie, “Morphology, genesis, and distribution of nanometer scale pores in siliceous mudstones of the Mississippian Barnett Shale,” *Journal of Sedimentary Research*, vol. 79, no. 12, pp. 848–861, 2009.
- [66] V. C. Hover, D. R. Peacor, and L. M. Walter, “Relationship between organic matter and authigenic illite/smectite in Devonian black shales, Michigan and Illinois Basins, USA,” in *Siliciclastic Diagenesis and Fluid Flow: Concepts and Applications*, L. J. Crossey, R. G. Loucks, and M. W. Totten, Eds., vol. 55 of Society for Sedimentary Geology, pp. 73–83, Special Publication, 1996.
- [67] C. Spötl and T. W. Vennemann, “Continuous-flow isotope ratio mass spectrometric analysis of carbonate minerals,” *Rapid Communications in Mass Spectrometry*, vol. 17, no. 9, pp. 1004–1006, 2003.
- [68] K. M. Révész and J. M. Landwehr, “ $\delta^{13}\text{C}$ and $\delta^{18}\text{O}$ isotopic composition of CaCO₃ measured by continuous flow isotope ratio mass spectrometry: statistical evaluation and verification by application to Devils Hole Core DH-11 calcite,” *Rapid Communications in Mass Spectrometry*, vol. 16, no. 22, pp. 2102–2114, 2002.
- [69] S. M. Sterner and R. J. Bodnar, “Synthetic fluid inclusions in natural quartz I. Compositional types synthesized and applications to experimental geochemistry,” *Geochimica et Cosmochimica Acta*, vol. 48, no. 12, pp. 2659–2668, 1984.
- [70] A. Fall and R. J. Bodnar, “How precisely can the temperature of a fluid event be constrained using fluid inclusions?,” *Economic Geology*, vol. 113, no. 8, pp. 1817–1843, 2018.
- [71] R. H. Goldstein and T. J. Reynolds, “Systematics of fluid inclusions in diagenetic minerals,” in *Society for Sedimentary Geology short course*, p. 199, Society for Sedimentary Geology, Tulsa, 1994.
- [72] R. H. Lander and S. E. Laubach, “Insights into rates of fracture growth and sealing from a model for quartz cementation in fractured sandstones,” *Geological Society of America Bulletin*, vol. 127, no. 3–4, pp. 516–538, 2015.
- [73] E. Ukar and S. E. Laubach, “Syn- and postkinematic cement textures in fractured carbonate rocks: insights from advanced cathodoluminescence imaging,” *Tectonophysics*, vol. 690, pp. 190–205, 2016.
- [74] I. S. Steward and P. L. Hancock, “Brecciation and fracturing within neotectonic normal fault zones of the Aegean region,” in *Deformation Mechanisms, Rheology and Tectonics*, R. J. Knipe and E. H. Rutter, Eds., vol. 54, pp. 105–112, Geological Society Special Publication, 1990.
- [75] H. Craig, “The measurement of oxygen isotope paleotemperatures,” in *Stable isotopes in oceanographic studies and paleotemperatures*, E. Tongiorgi, Ed., pp. 161–182, Consiglio Nazionale delle Ricerche, Pisa, 1965.
- [76] G. A. Shields, G. A. F. Carden, J. Veizer, T. Meidla, J.-Y. Rong, and R.-Y. Li, “Sr, C, and O isotope geochemistry of Ordovician brachiopods: a major isotopic event around the Middle-Late Ordovician transition,” *Geochimica et Cosmochimica Acta*, vol. 67, no. 11, pp. 2005–2025, 2003.
- [77] M. Steele-MacInnis, R. J. Bodnar, and J. Naden, “Numerical model to determine the composition of H₂O-NaCl-CaCl₂ fluid inclusions based on microthermometric and microanalytical data,” *Geochimica et Cosmochimica Acta*, vol. 75, no. 1, pp. 21–40, 2011.
- [78] J. Veizer, D. Ala, K. Azmy et al., “ $^{87}\text{Sr}/^{86}\text{Sr}$, $\delta^{13}\text{C}$ and $\delta^{18}\text{O}$ evolution of Phanerozoic seawater,” *Chemical Geology*, vol. 161, no. 1–3, pp. 59–88, 1999.
- [79] J. L. Banner, “Application of the trace element and isotope geochemistry of strontium to studies of carbonate diagenesis,” *Sedimentology*, vol. 42, no. 5, pp. 805–824, 1995.
- [80] E. Roedder, *Fluid Inclusions*, Mineralogical Society of America, Washington, D.C., 1984.
- [81] R. H. Goldstein, “Re-equilibration of fluid inclusions in low-temperature calcium-carbonate cement,” *Geology*, vol. 14, no. 9, pp. 792–795, 1986.
- [82] R. J. Bodnar, “Introduction to aqueous fluid systems,” in *Fluid Inclusions: Analysis and Interpretation*, I. Samson, A. Anderson, and D. Marshall, Eds., vol. 32, pp. 81–99, Mineral Association, Canada, 2003, Short Course.
- [83] A. Fall, P. Eichhubl, R. J. Bodnar, S. E. Laubach, and J. S. Davis, “Natural hydraulic fracturing of tight-gas sandstone reservoirs, Piceance Basin, Colorado,” *Geological Society of America Bulletin*, vol. 127, no. 1–2, pp. 61–75, 2015.
- [84] H. J. Corlett and B. Jones, “Petrographic and geochemical contrasts between calcite- and dolomite-filled burrows in the Middle Devonian Lonely Bay Formation, Northwest Territories, Canada: implications for dolomite formation in Paleozoic burrows,” *Journal of Sedimentary Research*, vol. 82, no. 9, pp. 648–663, 2012.
- [85] J. L. Banner, “Radiogenic isotopes: systematics and applications to earth surface processes and chemical stratigraphy,” *Earth-Science Reviews*, vol. 65, no. 3–4, pp. 141–194, 2004.
- [86] H. G. Machel and B. E. Buschkuehle, “Diagenesis of the Devonian Southesk-Cairn carbonate complex, Alberta, Canada: marine cementation, burial dolomitization, thermochemical sulfate reduction, anhydritization and squeeze fluid flow,” *Journal of Sedimentary Research*, vol. 78, no. 5, pp. 366–389, 2008.
- [87] P. A. Scholle and D. Ulmer-Scholle, “Cements and Cementation,” in *Sedimentology*, Encyclopedia of Earth Science, Springer, Dordrecht, 1978.
- [88] M. W. Longman, “Carbonate diagenetic textures from near-surface diagenetic environments,” *AAPG Bulletin*, vol. 64, pp. 461–487, 1980.
- [89] W. Zhaoming, Y. Haijun, Q. Yingmin, C. Yongquan, and X. Yanlong, “Ordovician gas exploration breakthrough in the Gucheng lower uplift of the Tarim Basin and its enlightenment,” *Natural Gas Industry B*, vol. 1, no. 1, pp. 32–40, 2014.
- [90] Y. Y. Zhang, H. Zwingmann, A. Todd, K. Liu, and X. Lou, “K-Ar dating of authigenic illites and its applications to study of oil-gas charging histories of typical sandstone reservoirs, Tarim Basin, Northwest China,” *Earth Science Frontiers*, vol. 11, pp. 637–647, 2004.
- [91] S. Shangguan, I. U. Peate, W. Tian, and Y. Xu, “Re-evaluating the geochronology of the Permian Tarim magmatic province: implications for temporal evolution of magmatism,” *Journal of the Geological Society*, vol. 173, no. 1, pp. 228–239, 2016.

- [92] X. Y. Zhang, J. Y. Gu, P. Luo, R. K. Zhu, and Z. Luo, "Genesis of the fluorite in the Ordovician and its significance to the petroleum geology of Tarim Basin," *Acta Petrologica Sinica*, vol. 22, no. 8, pp. 2220–2228, 2006.
- [93] E. Ukar, V. Baqués, S. E. Laubach, and R. Marrett, *Deep-seated, fault-related decameter-scale porosity in Ordovician carbonate rocks, Halahatang oilfield, Tarim Basin, China*, Journal of the Geological Society, 2020, Submitted to.
- [94] C. H. Moore, "Carbonate reservoirs: porosity evolution and diagenesis in a sequence stratigraphic framework," *Developments in Sedimentology*, vol. 55, p. 444, 2001.
- [95] H. G. Machel, "Effects of groundwater flow on mineral diagenesis, with emphasis on carbonate aquifers," *Hydrogeology Journal*, vol. 7, no. 1, pp. 94–107, 1999.
- [96] P. Muchez, M. Slobodnik, W. A. Viaene, and E. Keppens, "Geochemical constraints on the origin and migration of palaeofluids at the northern margin of the Variscan foreland, southern Belgium," *Sedimentary Geology*, vol. 96, no. 3–4, pp. 191–200, 1995.
- [97] C. Hill, "Sulfur redox reactions: Hydrocarbons, native sulfur, Mississippi Valley-type deposits, and sulfuric acid karst in the Delaware Basin, New Mexico and Texas," *Environmental Geology*, vol. 25, no. 1, pp. 16–23, 1995.
- [98] C. Cai, S. G. Franks, and P. Aagaard, "Origin and migration of brines from Paleozoic strata in Central Tarim, China: constraints from $^{87}\text{Sr}/^{86}\text{Sr}$, δD , $\delta^{18}\text{O}$ and water chemistry," *Applied Geochemistry*, vol. 16, no. 9–10, pp. 1269–1284, 2001.
- [99] C. Cai, K. Li, H. Li, and B. Zhang, "Evidence for cross formational hot brine flow from integrated $^{87}\text{Sr}/^{86}\text{Sr}$, REE and fluid inclusions of the Ordovician veins in Central Tarim, China," *Applied Geochemistry*, vol. 23, no. 8, pp. 2226–2235, 2008.
- [100] L. Jiang, R. H. Worden, C. F. Cai, A. Shen, and S. F. Crowley, "Diagenesis of an evaporite-related carbonate reservoir in deeply buried Cambrian strata, Tarim Basin, Northwest China," *AAPG Bulletin*, vol. 102, no. 1, pp. 77–102, 2017.
- [101] Z. Guo, Z. Zhang, C. Jia, and G. Wei, "Tectonics of Precambrian basement of the Tarim craton," *Science in China Series D: Earth Sciences*, vol. 44, no. 3, pp. 229–236, 2001.
- [102] S. Chaudhuri and N. Clauer, "Fluctuations of isotopic composition of strontium in seawater during the Phanerozoic Eon," *Chemical Geology*, vol. 59, pp. 293–303, 1986.
- [103] G. M. Anderson and G. Garven, "Sulfate sulfide-carbonate associations in Mississippi Valley-type lead-zinc deposits," *Economic Geology*, vol. 82, no. 2, pp. 482–488, 1987.
- [104] J. D. Cody, I. Hutcheon, and H. R. Krouse, "Fluid flow, mixing and the origin of CO_2 and H_2S by bacterial sulphate reduction in the Mannville Group, southern Alberta, Canada," *Marine and Petroleum Geology*, vol. 16, no. 6, pp. 495–510, 1999.
- [105] D. Y. Zhu, Z. J. Jin, and W. X. Hu, "Hydrothermal recrystallization of the Lower Ordovician dolomite and its significance to reservoir in northern Tarim Basin," *Science China Earth Sciences*, vol. 53, no. 3, pp. 368–381, 2010.
- [106] T. K. Kyser, N. P. James, and Y. Bone, "Shallow burial dolomitization and dedolomitization of Cenozoic cool-water limestones, southern Australia, geochemistry and origin," *Journal of Sedimentary Research*, vol. 72, no. 1, pp. 146–157, 2002.
- [107] S. C. George, T. E. Ruble, A. Dutkiewicz, and P. J. Eadington, "Assessing the maturity of oil trapped in fluid inclusions using molecular geochemistry data and visually-determined fluorescence colours," *Applied Geochemistry*, vol. 16, no. 4, pp. 451–473, 2001.
- [108] J. Guo, "Buried-hill paleokarst and its control on reservoir heterogeneity in Ordovician, Lunnan region of Tarim Basin," *Acta Sedimentologica Sinica*, vol. 11, pp. 56–64, 1993.
- [109] X. Ni, L. Zhang, A. Shen, L. Han, Z. Qiao, and K. Zhao, "Characteristics and genesis of Ordovician carbonate karst reservoir in Yingmaili-Halahatang area, Tarim Basin," *Acta Sedimentologica Sinica*, vol. 29, pp. 465–474, 2011.
- [110] M. R. Saltzman and S. A. Young, "Long-lived glaciation in the Late Ordovician? Isotopic and sequence-stratigraphic evidence from western Laurentia," *Geology*, vol. 33, no. 2, pp. 109–112, 2005.
- [111] H. QU, Z. WANG, H. YANG, Y. ZHANG, H. YU, and X. WANG, "Karstification of reef-bank facies carbonate and its control on pore distribution: A case study of Upper Ordovician Lianglitage Formation in eastern Tazhong area, Tarim Basin, NW China," *Petroleum Exploration and Development*, vol. 40, no. 5, pp. 592–598, 2013.
- [112] W. Yang, M. Hu, and L. Zhang, "Identification method of Ordovician ancestral river system in Halahatang area, north Tarim Basin," in *2014 IEEE Workshop on Electronics, Computer and Applications*, pp. 672–674, Ottawa, ON, Canada, May 2014.
- [113] J. Gu, J. Jia, and H. Fang, "Reservoir characteristics and genesis of high-porosity and high-permeability reservoirs in Tarim Basin," *Chinese Science Bulletin*, vol. 47, Supplement 1, pp. 12–19, 2002.
- [114] G. Zhu, A. V. Milkov, Z. Zhang et al., "Formation and preservation of a giant petroleum accumulation in superdeep carbonate reservoirs in the southern Halahatang oil field area, Tarim Basin, China," *AAPG Bulletin*, vol. 103, no. 7, pp. 1703–1743, 2019.
- [115] S. W. Tinker, J. R. Ehrets, and M. D. Brondos, "Multiple karst events related to stratigraphic cyclicity: San Andres Formation, Yates field, West Texas," in *Unconformities and Porosity in Carbonate Strata*, D. A. Budd, A. H. Saller, and P. M. Harris, Eds., vol. 63 of AAPG Memoir, pp. 213–237, 1995.
- [116] R. A. Nelson, *Geologic Analysis of Naturally Fractured Reservoirs*, Gulf Publishing Co., Houston, 1985.
- [117] W. Narr, D. S. Schechter, and L. B. Thompson, *Naturally Fractured Reservoir Characterization*, vol. 112, Society of Petroleum Engineers, Richardson, Texas, 2006.
- [118] S. E. Laubach, R. H. Lander, L. J. Criscenti et al., "The role of chemistry in fracture pattern development and opportunities to advance interpretations of geological materials," *Reviews of Geophysics*, vol. 57, no. 3, pp. 1065–1111, 2019.
- [119] S. N. Ehrenberg, O. Walderhaug, and K. Bjørlykke, "Carbonate porosity creation by mesogenetic dissolution: reality or illusion?," *AAPG Bulletin*, vol. 96, no. 2, pp. 217–233, 2012.
- [120] S. N. Ehrenberg, "Porosity destruction in carbonate platforms," *Journal of Petroleum Geology*, vol. 29, no. 1, pp. 41–52, 2006.
- [121] D. B. Ma, G. H. Wu, N. Scarselli, X. S. Luo, J. F. Han, and Z. Y. Chen, "Seismic damage zone and width-throw scaling along the strike-slip faults in the Ordovician carbonates in the Tarim Basin," *Petroleum Science*, vol. 16, no. 4, pp. 752–762, 2019.